UNITED NATIONS EDUCATIONAL, SCIENTIFIC AND CULTURAL ORGANIZATION
INTERNATIONAL CENTRE FOR THEORETICAL PHYSICS
I.C.T.P., P.O. BOX 586, 34100 TRIESTE, ITALY, CABLE: CENTRATOM TRIESTE

SMR.703 - 16

WORKING PARTY ON
MECHANICAL PROPERTIES OF INTERFACES

23 AUGUST - 3 SEPTEMBER 1993

"Interfaces: Structure and Properties" (Part IV)

"Role of Interface Dislocations and Surface Steps in the Work of Adhesion"

Dieter WOLF
Materials Science Division
Argonne National Laboratory
9700 S. Cass. Avenue
Building 233
Argonne, IL 60439
U.S.A.

CHAPTER TWENTY-SIX

Role of interface dislocations and surface steps in the work of adhesion

D. Wolf and J. A. Jaszczak

Introduction · Interfacial decohesion: from interface dislocations to surface steps · Computer simulations · Core and elastic strain-field effects in free surfaces and GBs · A broken-bond model for interfacial decohesion · Summary and conclusions

26.1 INTRODUCTION

Although crack extension is usually accompanied by plasticity and other highly complex, non-equilibrium kinetic phenomena, the ideal brittle-fracture energy nevertheless represents a useful lower thermodynamic limit for the work of adhesion, W^{ad}, particularly since it is often assumed that both the plastic work and the energy due to kinetic processes increase in proportion with W^{ad} [1]. Brittle interfacial decohesion in the sense of Griffith [2], i.e. the reversible transformation of an internal interface into two free surfaces, hence requires as a minimum an understanding of the equilibrium energies of the initial and final states, from which the ideal cleavage-fracture energy,

$$W^{ad} = \gamma_1 + \gamma_2 - \varepsilon \tag{26.1}$$

can be determined. Here the energy of the internal interface is denoted by ε, while the two free-surface energies are denoted by γ_1 and γ_2, respectively. To elucidate ideal-cleavage decohesion of internal interfaces hence necessitates a better understanding, from a common viewpoint, of the energies of internal interfaces and external surfaces. In the following, by investigating the zero-temperature work of adhesion, we hope to develop such a unified framework.

Much of the high-resolution-microscopy work of recent years has shown that the structure of internal interfaces generally consists of areas of localized misfit, so-called misfit **dislocations**, which are separated by elastically strained regions of relatively good match across the interface [1, 3–5]. Similarly, the structure of free surfaces is usually characterized in terms of localized **steps** or **ledges** which are separated by regions of 'flat' surface material [6]. The ideal-cleavage decohesion of an internal interface into two free surfaces may hence be viewed as the reversible transformation of misfit dislocations into surface steps. Since both interface dislocations and surface steps consist of highly distorted core regions surrounded by elastic strain fields, interfacial decohesion therefore involves the transformation of dislocation cores into the cores of surface steps, and of the long-range elastic strain fields near dislocations into the much shorter-ranged strain fields surrounding the surface steps. It is the purpose of this chapter to investigate the underlying core and elastic phenomena accompanying this transformation by means of atomistic computer simulations.

Introduction

Without loss of generality, throughout this chapter we will consider the decohesion of grain boundaries (GBs) as simple model systems for elucidating the transformation of dislocations into steps. As discussed, for example, in Chapter 1 of this volume [7], GBs generally have **five** macroscopic degrees of freedom (DOFs), i.e. three more than free surfaces (with only the two DOFs associated with the surface normal, $\hat{n}$). However, to emphasize the geometrical similarity between GBs and free surfaces, these DOFs will be chosen such that **four** are associated with the GB-plane normal, characterized by the unit vectors $\hat{n}_1$ and $\hat{n}_2$ in the two halves of the bicrystal (corresponding to the two fracture surfaces obtained upon decohesion), while the remaining one is represented by the twist angle, θ. A non-vanishing value of θ adds a twist component (i.e. screw dislocations) to the GB, in addition to the tilt component (i.e. edge dislocations) already present once the GB plane has been fixed. Then, to focus on the similarity between surface steps and **edge** dislocations (to be elaborated upon below), but yet still capture the essential core and elastic phenomena involved, we limit ourselves to the following two types of GBs whose structure contains edge dislocations only.

1. By investigating pure **tilt** boundaries, from the outset the twist component is eliminated altogether. Like free surfaces, the GBs are fully characterized by only the DOFs associated with the interface plane (four in the case of asymmetrical tilt GBs, and two in the symmetrical case). Their dislocation structure should therefore be most intimately connected with the structure of the steps in the corresponding fracture surfaces.
2. For large twist angles, θ, in the Read–Shockley sense [8], the cores of the **screw** dislocations overlap completely, and a simple model may be formulated in which all interactions across the interface are assumed to be entirely random. This model of a 'random grain boundary' (RGB) [9–11] thus represents an idealized theoretical model suitable for **high-angle twist** boundaries.

Because in the RGB model the twist angle is eliminated as a DOF, both pure tilt boundaries and RGBs are characterized fully by only the DOFs associated with the GB plane. However, in the RGB model screw dislocations – albeit with completely overlapping cores – are, in principle, present. A comparison of the work of adhesion of RGBs with that of pure tilt boundaries should therefore elucidate the role of screw dislocations in the transformation of interfacial edge dislocations into surface steps.

Given that (i) the appearance of steps in surfaces is directly connected with the crystallographic orientation of the surface **plane** and (ii) the strictly edge-type dislocations in both of the above types of GBs are fully characterized solely by the DOFs associated with the GB **plane**, a comparison of the energies and structures of these GBs with those of free surfaces should also provide insight into the importance of the role of the interface plane in the work of adhesion. Moreover, since the bulk **ideal-crystal** brittle-fracture energy, 2γ (eq. (26.1)) is also a very sensitive function of the fracture plane, such a comparison of free surfaces and GBs also provides information on the crystallographic anisotropy of the perfect-crystal cleavage energy.

Two conceptually different types of interatomic potentials will be used in our computer simulations. To provide some insight into the role of many-body effects, results obtained via a semi-empirical many-body embedded-atom-method (EAM) potential [12] will be compared with simulations involving a conceptually simpler Lennard–Jones (LJ) pair potential. EAM potentials have the advantage over pair potentials that they incorporate, at least conceptually, the many-body nature of metallic bonding, while being relatively efficient computationally. In these potentials the strength of the interaction between atoms depends on the local volume or, in another interpretation, on the local electron density 'sensed' by every atom. Also, while at zero temperature any equilibrium pair potential automatically satisfies the Cauchy relation for the elastic constants, $C_{12} = C_{44}$, these many-body potentials permit all three elastic constants of a cubic metal to be determined (or used in the fitting). An iterative energy-minimization algorithm ('lattice statics') is used to compute the fully

relaxed zero-temperature atomic structure and energy of free surfaces and GBs, including the volume expansion at the internal interfaces [13, 14].

It should be noted that the absolute values of GB and free-surface energies presented throughout this chapter are probably not very reliable. Even for the many-body potentials there exist discrepancies (in some cases up to a factor of two [12]) between the computed free-surface energies, on the one hand, and the values obtained from experiments and by means of electronic-structure methods on the other. We nevertheless believe that a comparison of the **relative** energies of GBs and free surfaces is meaningful, particularly when the same generic behavior is obtained by means of conceptually different interatomic potentials.

The chapter is organized as follows. In section 26.2 we offer a formal description of the work of adhesion for symmetrical tilt boundaries (STGBs) in terms of the line energies of the underlying edge dislocations and surface steps, including their elastic interactions. In section 26.3, our computer-simulation results for the energies of STGBs, the RGB model and free surfaces will be compared, including the work of adhesion of the internal interfaces. An analysis of the crystallographic anisotropy of the work of adhesion is also presented in section 26.3. This systematic investigation of the role of the interface plane in ideal cleavage decohesion leads naturally to the distinction between 'special', 'vicinal', and 'high-angle' interfaces, with qualitatively rather different behaviors of the work of adhesion. Then, in section 26.4 the core and elastic-interaction energies of steps and dislocations are determined directly by considering in detail the energies of STGBs and surfaces in the vicinity of two energy cusps. Finally, in section 26.5 it is shown that only the cores of the steps and dislocations, but not their surrounding strain fields, give rise to broken bonds; this finding leads naturally to an elucidation of the role of broken bonds in interfacial decohesion and, hence, the intrinsic limitations of broken-bond and structural-unit models.

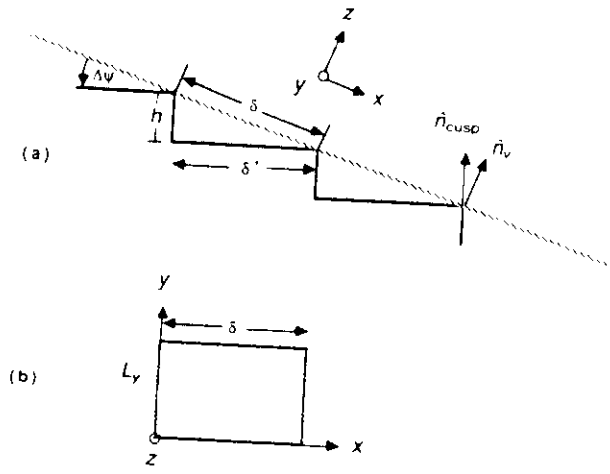

Fig. 26.1 Orientation of a 'vicinal' surface (i.e. one containing steps of height h [6, 7]), with unit normal $\hat{n}_v$ which is rotated by the angle $\Delta\psi$ relative to a 'special' surface (i.e. one giving rise to an energy cusp), with unit normal $\hat{n}_{cusp}$. In both (a) and (b), the vicinal surface is assumed to lie in the x–y plane, with the surface normal defining the z direction. While (a) shows a view down the y axis (i.e. parallel to the steps), (b) represents a view onto the x–y plane, with the steps, separated by the distance δ, forming the left and right edges of the planar unit cell.

26.2 INTERFACIAL DECOHESION: FROM INTERFACE DISLOCATIONS TO SURFACE STEPS

26.2.1 Surface steps

With only the two macroscopic DOFs associated with the surface normal, free surfaces conceptually represent the simplest of all planar defects (Chapter 1 in this volume [7]). Given that these two DOFs are usually chosen to represent the orientation of the surface normal, the appearance of steps in surfaces is clearly connected with the crystallographic orientation of the surface **plane**. Figure 26.1 illustrates the orientation of a 'vicinal' surface (i.e. one containing steps [6, 7]), with unit normal $\hat{n}_v$, relative to a 'special' surface (i.e. one giving rise to an energy cusp), with unit normal $\hat{n}_{cusp}$. In both Figs. 26.1(a) and (b), the vicinal surface is assumed to lie in the x–y-plane, with the surface normal defining the z-direction. While Fig. 26.1(a) shows a view down the y-axis (i.e. parallel to the steps), Fig. 26.1(b) represents a view onto the x–y-plane, with the steps, separated by the dis-

tance δ, forming the left and right edges of the planar unit cell.

According to the figure, the detailed geometry of the steps in the vicinal surface may be described in terms of a rotation of the unit vector $\hat{n}_{cusp}$ about an axis perpendicular to both $\hat{n}_{cusp}$ and $\hat{n}_v$ by the angle $\Delta\psi$; the latter is obviously determined by the dot product

$$\cos \Delta\psi = (\hat{n}_v \cdot \hat{n}_{cusp}) \tag{26.2}$$

Thus, the spacing, δ, between the steps of height h is given by

$$\delta = h/\sin \Delta\psi \tag{26.3}$$

If one assumes the increased energy of the vicinal surface to be entirely due to the introduction of steps into the cusped surface, its energy per unit area, $\gamma_v \equiv \gamma(\Delta\psi)$, may be written as follows [15]:

$$\gamma(\Delta\psi) = [\gamma_{cusp} A_{cusp} + \Gamma(\delta)L_v]/A(\Delta\psi) \tag{26.4}$$

The second contribution on the right-hand side represents the total line energy of the steps per unit surface area, with $\Gamma(\delta)$ denoting the energy per unit length of the steps (i.e. their line energy) and L_v representing the total step length in the planar unit cell (Fig. 26.1(b)). Because of the interaction between neighboring steps, the line energy Γ is a function of their distance δ. The first contribution to $\gamma(\Delta\psi)$ in eq. (26.4) arises from the energy of the cusped surface, $\gamma_{cusp} \equiv \gamma(\Delta\psi = 0)$, reduced however by its projection onto the larger planar unit-cell area, $A(\Delta\psi)$, of the vicinal surface relative to the unit-cell area, $A_{cusp} = A(\Delta\psi = 0)$, of the cusped orientation. As seen from Fig. 26.1(b), $A(\Delta\psi)$ is given by

$$A(\Delta\psi) = L_v\delta = L_v h/\sin \Delta\psi \tag{26.5}$$

from which it follows that

$$A_{cusp}/A(\Delta\psi) = \delta'/\delta = \cos \Delta\psi \tag{26.6}$$

with δ' defined in Fig. 26.1(a).

Inserting eqs. (26.5) and (26.6) into eq. (26.4), and using eq. (26.3) to replace $\Delta\psi$ by δ, we obtain:

$$\gamma(\delta) - \gamma_{cusp}(1 - h^2/\delta^2)^{\frac{1}{2}} = \Gamma(\delta)/\delta \tag{26.7a}$$

Sometimes it is more convenient to express γ directly in terms of $\Delta\psi$ and write instead:

$$\gamma(\Delta\psi) - \gamma_{cusp} \cos \Delta\psi = [\Gamma(\delta)/h] \sin \Delta\psi \tag{26.7b}$$

As discussed further in section 26.4.1, the mutual repulsion between steps arising from their overlapping elastic strain fields may formally be incorporated in eqs. (26.7(a)) and (b) by decomposing the line energy Γ as follows:

$$\Gamma(\delta) = \Gamma^{\infty}_{core} + \Gamma_{el}(\delta) \tag{26.8}$$

where Γ^{∞}_{core} and Γ_{el} represent, respectively, the 'core' and strain-field (i.e. elastic) energies of the step. In writing eq. (26.8), it was assumed that only the elastic contribution to the line energy varies as a function of δ while the core energy of the steps is essentially independent of δ. The validity of this assumption will be tested in section 26.4.1.

The elastic energy in eq. (26.8) may be broken down further into the line energies of isolated (i.e. non-interacting) steps, $\Gamma^{\infty}_{el} = \Gamma_{el}(\delta \to \infty)$, and the step–step interaction energy, $\Gamma^{s-s}_{el}(\delta)$, according to

$$\Gamma_{el}(\delta) = \Gamma^{\infty}_{el} + \Gamma^{s-s}_{el}(\delta) \tag{26.9}$$

As illustrated schematically in Fig. 26.2, the elastic step–step interaction energy is determined by the (shaded) area of overlap of the elastic displacement fields surrounding each individual step, and therefore varies as a function of δ. According to Marchenko and Parshin [16], the consequent elastic **repulsion** between two identical steps decreases inversely with the square of their distance, according to

$$\Gamma^{s-s}_{el}(\delta) = G^{s-s}_{el}/\delta^2 \tag{26.10}$$

where G^{s-s}_{el} is a constant characterizing the elastic strength of the step–step interaction. Inserting eqs. (26.8)–(26.10) into eq. (26.7(a)), we thus obtain:

$$\gamma(\delta) - \gamma_{cusp}(1 - h^2/\delta^2)^{\frac{1}{2}} = \Gamma^{\infty}/\delta + G^{s-s}_{el}/\delta^3 \tag{26.11a}$$

where Γ^{∞} contains the δ-independent contributions, according to

$$\Gamma^{\infty} = \Gamma^{\infty}_{core} + \Gamma^{\infty}_{el} \tag{26.12}$$

By definition the line energy of an isolated step, Γ^{∞}, thus includes contributions from both the fully

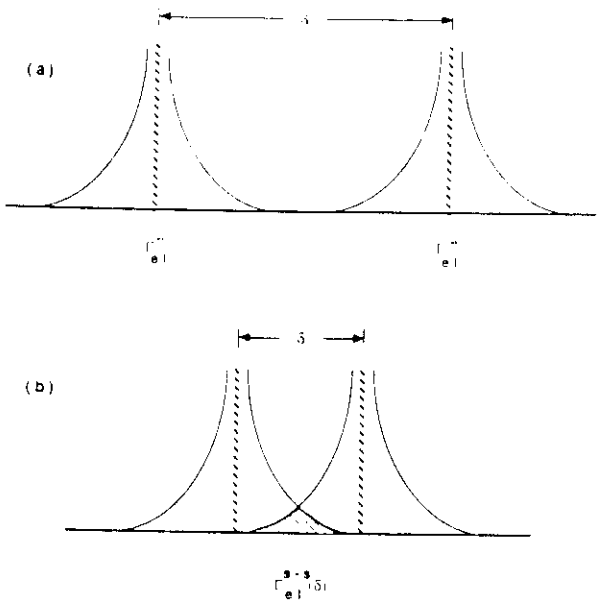

Fig. 26.2 Elastic strain fields between steps (schematic). (a) Non-interacting limit (for large separations δ) in which the strain fields do not overlap. (b) The interaction between steps is given by the area of overlap between the strain fields of neighboring steps.

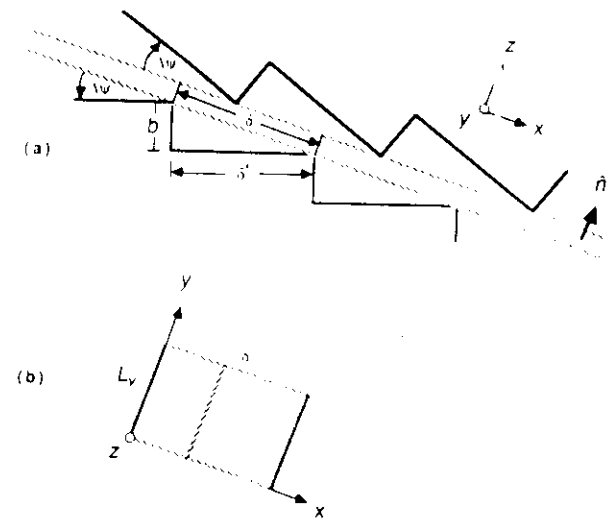

Fig. 26.3 Conceptually a symmetrical tilt grain boundary (STGB) may be formed by bringing two identical free surfaces into contact, thus transforming the two parallel sets of surface steps, each of height h, into two parallel sets of edge dislocations, each with Burger's vector $\boldsymbol{b}$ (compare Fig. 26.1). In forming such a tilt bicrystal, the relative positions of its two halves, characterized by the rigid-body-translation vector $\boldsymbol{T} = (T_x, T_y, T_z)$, are variables.

relaxed cores and elastic displacement fields of the steps, while $\Gamma_{el}^{s-s}(\delta)$ arises solely from the displacement fields (Fig. 26.2).

Instead of expressing the elastic energy directly as a function of δ, it may alternatively be expressed as a function of $\Delta\psi$, i.e. $\Gamma(\delta) \rightarrow \Gamma(\Delta\psi)$; eq. (26.3). Equations (26.8)–(26.10) may then, instead, be written as follows

$$\Gamma(\Delta\psi) = \Gamma_{core} + \Gamma_{el}(\Delta\psi) \quad (26.13)$$

$$\Gamma_{el}(\Delta\psi) = \Gamma_{el}^{\infty} + \Gamma_{el}^{s-s}(\Delta\psi) \quad (26.14)$$

$$\Gamma_{el}^{s-s}(\Delta\psi) = (G_{el}^{s-s}/h^2)\sin^2\Delta\psi \quad (26.15)$$

and eq. (26.11a) becomes (eq. (26.7b)):

$$\gamma(\Delta\psi) - \gamma_{cusp}\cos\Delta\psi = (\Gamma^{\infty}/h)\sin\Delta\psi + (G_{el}^{s-s}/h^3)\sin^3\Delta\psi \quad (26.11b)$$

The validity of eqs. (26.11(a)) and (b), and the assumptions made in their derivation, will be tested in some detail in section 26.4.1.

26.2.2 Interface dislocations

It is interesting to observe the geometrical similarity of this picture of a vicinal-free surface with the geometry of an STGB. As illustrated in Fig. 26.3, an STGB may conceptually be formed by bringing two identical free surfaces into contact, thus transforming the two parallel sets of surface steps, each of height h, into two parallel sets of edge dislocations, each with Burger's vector $\boldsymbol{b}$. In forming such a tilt bicrystal, the relative positions of its two halves are obviously variables. The three components of the related rigid-body translation vector, $\boldsymbol{T} = (T_x, T_y, T_z)$, are known as the three microscopic or translational DOFs of the GB [17]; in practice they are governed by the condition that the bicrystal be in a state of minimum free energy or, at least, in a metastable translational state for a given choice of the macroscopic DOFs.

Assuming some arbitrary, but well-defined rigid-body translation to be present at the GB, in analogy to eq. (26.7a) the energy per unit area, $\varepsilon(\Delta\psi)$, of a 'vicinal' GB (i.e. one in the vicinity of a 'special' or 'cusped' GB which, by this definition, is entirely dislocation free) may be written as follows (Figs. 26.1 and 26.3):

$$\varepsilon(\delta) - \varepsilon_{cusp}(1 - h^2/\delta^2)^{\frac{1}{2}} = 2\Lambda(\delta)/\delta \qquad (26.16a)$$

or, in analogy to eq. (26.7b),

$$\varepsilon(\Delta\psi) - \varepsilon_{cusp}\cos\Delta\psi = 2[\Lambda(\delta)/b]\sin\Delta\psi \qquad (26.16b)$$

where ε_{cusp} is the energy per unit area of the cusped GB while $\Lambda(\delta)$ denotes the total energy per unit length of the dislocations, i.e. their total line energy. Notice that in writing eq. (26.16b), the step height, h, in eq. (26.7b) was replaced by the magnitude of the Burger's vector, $\boldsymbol{b}$ (Fig. 26.3(a)).

If the tilt boundary in Fig. 26.3 were asymmetrical, the two sets of edge dislocations would still be parallel to the tilt axis; however, their spacings, δ_1 and δ_2 (which are related to angles $\Delta\psi_1$ and $\Delta\psi_2$), and Burgers vectors, $\boldsymbol{b}_1$ and $\boldsymbol{b}_2$, would now differ, and eqs. (26.16a,b), would have to be modified accordingly.

As in the case of the steps, the mutual repulsion between dislocations arising from their overlapping elastic strain fields may formally be incorporated in eq. (26.16) by decomposing Λ as follows (eq. (26.8)):

$$\Lambda(\delta) = \Lambda^{\infty}_{core} + \Lambda_{el}(\delta) \qquad (26.17)$$

where Λ^{∞}_{core} and Λ_{el} represent, respectively, the core and elastic strain-field energies of the two sets of dislocations. As for the steps, in writing eq. (26.17) it was assumed that only the elastic contribution to the line energy depends on δ while the dislocation-core energy is essentially independent of their spacing, an assumption to be tested in section 26.4.2.

The elastic energy in eq. (26.17) may be broken down further into the line energy of an isolated (i.e. non-interacting) dislocation, $\Lambda^{\infty}_{el} = \Lambda_{el}(\delta \to \infty)$, and the energy of interaction between different dislocations, $\Lambda^{d-d}_{el}(\delta)$, according to (Fig. 26.2)

$$\Lambda_{el}(\delta) = \Lambda^{\infty}_{el} + \Lambda^{d-d}_{el}(\delta) \qquad (26.18)$$

As in the case of the steps, the latter is determined by the area of overlap of the elastic displacement fields surrounding each individual dislocation, and therefore varies as a function of δ. According to Read and Shockley [8], the dislocation–interaction energy depends logarithmically on their distance, according to

$$\Lambda^{d-d}_{el}(\delta) = -L^{d-d}_{el}\ln(b/\delta) \qquad (26.19)$$

where the constant L^{d-d}_{el} characterizes the elastic strength of this repulsive interaction. Inserting eqs. (26.17)–(26.19) into eq. (26.16a), analogous to eq. (26.11a) we obtain:

$$\varepsilon(\delta) - \varepsilon_{cusp}(1 - h^2/\delta^2)^{\frac{1}{2}} = 2[\Lambda^{\infty}/\delta - (L^{d-d}_{el}/\delta)\ln(b/\delta)] \qquad (26.20a)$$

where Λ^{∞} contains the δ-independent contributions, according to (compare eq. (26.12))

$$\Lambda^{\infty} = \Lambda^{\infty}_{core} + \Lambda^{\infty}_{el} \qquad (26.21)$$

As is well known, the elastic contribution to the line energy of an isolated lattice dislocation in an infinite crystal, Λ^{∞}_{el}, diverges whereas the core contribution, Λ^{∞}_{core}, remains finite. However, for the long-range-ordered arrays of dislocations in GBs (with mutually opposite Burger's vectors; Fig. 26.3), these divergences in the far-away strain fields of the individual dislocations cancel one another, with a consequently finite and small residual value of Λ^{∞}_{el} determined by the geometry of the array. The line energy in eq. (26.21) is therefore probably dominated by that of the dislocation **cores**. Interestingly, the total line energy of the steps in eq. (26.12) is also dominated by the core energy; however, for an entirely different reason, namely the weakness of the step–step interaction (section 26.4.1 below). A comparison of the line energies of steps and dislocations therefore provides mostly information on the related core energies while the information on their elastic displacement fields is largely contained in the interaction-energy term, i.e. the magnitudes of G^{s-s}_{el} and L^{d-d}_{el}.

As for the steps, eq. (26.20a) may alternatively be

written in terms of $\Delta\psi$ as follows (eqs. (26.16b) and (26.11b)):

$$\varepsilon(\Delta\psi) - \varepsilon_{cusp}\cos\Delta\psi = 2[(\Lambda^{s}/b)\sin\Delta\psi - (L_{el}^{d-d}/b)\sin\Delta\psi\ \ln(\sin\Delta\psi)] \quad (26.20b)$$

The validity of eqs. (26.20a,b), and the assumptions made in their derivation, will be tested in some detail in section 26.4.2.

26.2.3 Work of adhesion

If we assume that the free surfaces in Fig. 26.1 and the STGBs in Fig. 26.3 show energy cusps for the same special crystallographic planes (an assumption to be tested below), eqs. (26.11) and (26.20) may be inserted into eq. (26.1) to obtain the ideal cleavage-fracture energy,

$$W^{ad}(\delta) = (2\gamma_{cusp} - \varepsilon_{cusp})(1 - h^2/\delta^2)^{\frac{1}{2}} + 2(\Gamma^{s} - \Lambda^{s})/\delta + (2/\delta)[G_{el}^{s-s}/\delta^2 + L_{el}^{d-d}\ln(b/\delta)] \quad (26.22a)$$

or, in terms of $\Delta\psi$,

$$W^{ad}(\Delta\psi) = (2\gamma_{cusp} - \varepsilon_{cusp})\cos\Delta\psi + 2(\Gamma^{s}/h - \Lambda^{s}/b)\sin\Delta\psi + 2\sin\Delta\psi[(G_{el}^{s-s}/h^3)\sin^2\Delta\psi + (L_{el}^{d-d}/b)\ln(\sin\Delta\psi)] \quad (26.22b)$$

According to these expressions, a high cleavage energy therefore requires (i) a large difference in the cusped energies, $2\gamma_{cusp} - \varepsilon_{cusp}$, and/or (ii) a large line energy of the steps compared to that of the dislocations, and/or (iii) a high elastic energy of interaction between steps by comparison with dislocations. For a better understanding of the work of adhesion it is therefore necessary to investigate the core and elastic properties of steps and dislocations.

Finally, exactly at the cusp (i.e. for $\Delta\psi = 0$, or $\delta \to \infty$), eqs. (26.22a,b) reproduce the trivial result that for a symmetrical GB,

$$W^{ad}(\Delta\psi = 0) = (2\gamma_{cusp} - \varepsilon_{cusp}) \quad (26.23)$$

Because the cusped surfaces and interfaces are free of steps and dislocations, respectively, the related work of adhesion therefore provides no information on either the line energies of steps and dislocations or on their interaction.

26.2.4 Distinction between 'special', 'vicinal', and 'high-angle' interfaces

The above discussion illustrates the distinct effects due to the cores and elastic strain fields of interface dislocations and surface steps in the work of adhesion. These effects lead naturally to a distinction between three types of interfaces, with a rather different physical behavior as far as the work of adhesion is concerned. In analogy to the distinction between low- and high-angle GBs, we distinguish 'vicinal' interfaces, whose work of adhesion is governed by both the elastic and the core effects, from 'high-angle' interfaces, in which the core effects dominate completely. Because they are entirely free of dislocations or steps, the 'special' interfaces represent a class all by themselves; similar to the 'high-angle' interfaces, however, no elastic effects therefore contribute to their work of adhesion.

Since the distinction between special and vicinal interfaces was discussed earlier in this section, here we only consider further what we refer to as the 'high-angle' interfaces. Because in these interfaces the cores of the dislocations and of the corresponding surface steps overlap, their work of adhesion can be expected to be dominated by the core energies. Given that (i) the elastic interaction between line defects is mediated by the strained perfect-crystal-like regions between them, and (ii) virtually no such regions remain when the cores overlap, the interaction energies, $\Gamma_{el}^{s-s}(\delta)$ and $\Lambda_{el}^{d-d}(\delta)$, should vanish as $\delta \to h$ or $\delta \to b$, respectively (i.e. for $\Delta\psi \to 90°$; eq. (26.2) and Figs. 26.1 and 26.3). While the Read–Shockley equation (26.19) automatically satisfies this requirement, the Marchenko–Parshin expression (26.10) approaches a finite value of G_{el}^{s-s}/h^2. In our further analysis of high-angle interfaces, this unphysical prediction of eq. (26.10) will be corrected by eliminating this remaining, finite-energy elastic energy for $\delta \to h$ from the relevant expressions.

Ignoring thus all effects arising from the elastic

strain fields near the steps and dislocations, the expressions derived in sections 26.2.1–26.2.3 simplify considerably. For example, the free-surface energy in eqs. (26.11a,b) becomes

$$\gamma_{\text{core}} \equiv \gamma(\Delta\psi = 90°) = \Gamma^{x}_{\text{core}}/h \qquad (26.24)$$

while the GB energy in eqs. (26.20a,b) simplifies as follows:

$$\varepsilon_{\text{core}} \equiv \varepsilon(\Delta\psi = 90°) = 2\Lambda^{x}_{\text{core}}/b \qquad (26.25)$$

The ratio,

$$f_c \equiv \varepsilon_{\text{core}}/2\gamma_{\text{core}} = (\Lambda^{x}_{\text{core}}/b)/(\Gamma^{x}_{\text{core}}/h) \qquad (26.26)$$

therefore provides a direct measure for the relative magnitudes of the **core** energies of isolated steps and dislocations. As illustrated in section 26.4, the simulation of free surfaces and STGBs far away from any of the energy cusps permits determination of f_c. The above relations yield the following expression for the work of adhesion:

$$W^{\text{ad}}_{\text{core}} \equiv W^{\text{ad}}(\Delta\psi = 90°) = 2(\Gamma^{x}_{\text{core}}/h - \Lambda^{x}_{\text{core}}/b) \qquad (26.27)$$

Equations (26.24)–(26.27) have two noteworthy properties. First, a positive work of adhesion implies automatically that the core energy of the steps exceeds that of the dislocations. As discussed in the next section, this requirement finds a natural explanation within the framework of a broken-bond model. Second, the energies of the cusped surfaces and GBs are remarkably absent in all three, i.e. the energy and the ideal cleavage-fracture energy of a high-angle interface do not depend on the energies of any of the cusped orientations, and neither do the energies of the related free surfaces. Instead, these energies are governed solely by the core energies of the underlying line defects and by the magnitude of the geometrical discontinuity at the line defects (i.e. the step height and Burger's vector). The ratio,

$$f_{\text{ad}} \equiv W^{\text{ad}}_{\text{core}}/2\gamma_{\text{core}} = 1 - (\Lambda^{x}_{\text{core}}/b)/(\Gamma^{x}_{\text{core}}/h) = 1 - f_c \qquad (26.28)$$

therefore provides another direct measure for the relative magnitudes of the core energies of steps and dislocations.

26.2.5 Role of broken bonds

Broken-bond models have been used for the calculation of surface energies with a great a deal of success for at least 50 years [6]. Such models naturally give rise to cusps in energy-orientation plots and lead to faceted crystal shapes [6]. Since broken-bond models do not take into account elastic-interaction effects, it appears that such effects are small for surfaces – an assumption that will be quantified in section 26.4.1. Broken-bond models can also be useful in predicting structure–property correlations in GBs [18]. While, based on the Read–Shockley model [8], elastic-interaction effects are expected to be important in the GB case, broken-bond models are nevertheless useful in predicting the energy contributions of the cores, since it is only the dislocation cores which contribute to miscoordination but not their elastic strain fields (for details see section 26.6).

The coordination coefficient, $C(\alpha, \hat{n})$, for the α-th nearest neighbors (*nn*), defined by [19]

$$C(\alpha, \hat{n}) = \sum_{n} |K_{\text{id}}(\alpha) - K_n(\alpha, \hat{n})|/A(\hat{n}) \qquad (\alpha = 1, 2, \ldots) \qquad (26.29)$$

represents a convenient measure per unit area of how well, on average, an interface of orientation $\hat{n}$ is coordinated (or, perhaps better, miscoordinated). Here $A(\hat{n})$ is the planar unit-cell area (assuming, for convenience, that the interface is commensurate [7]); the dimensions of $C(\alpha, \hat{n})$ are therefore $(\text{length})^{-2}$, and its values are usually given in units of a^{-2}, where a is the lattice parameter. We define as α-th neighbors all those atoms n within a minimum radius $(R_\alpha + R_{\alpha-1})/2$ and a maximum radius of $(R_{\alpha+1} + R_\alpha)/2$ of a given atom, i.e. all atoms within a radius half way between corresponding neighboring shells. R_α here denotes the radius of the α-th *nn* shell in a perfect crystal. For every atom we thus determine the deviation, $\Delta K_n(\alpha, \hat{n}) = K_{\text{id}}(\alpha) - K_n(\alpha, \hat{n})$, of its number of α-th nearest neighbors from that of a perfect fcc crystal, $K_{\text{id}}(\alpha)$, and subsequently summing over the absolute values. For $\alpha = 1$, all atoms between $R_0 = 0$ and the half-way point

between nearest and 2nd-nearest neighbors are included [19].

To illustrate eq. 26.29, by an example, we consider unrelaxed free surfaces in monatomic structures for which the miscoordination in eq. (26.29) may be given analytically as a function of the orientation $\hat{n}$ as follows [6]:

$$C^{\mathrm{surf}}(\alpha, \hat{n}) = (\rho/2) \sum_{i} |\hat{n} \cdot \boldsymbol{B}(\alpha)_i| \qquad (26.30)$$

where the $\boldsymbol{B}(\alpha)_i$ are the 'bond vectors' from an atom to its α-th neighbors, and ρ is the number of atoms per volume; the summation over i involves all the neighbors of type α. For example, for surfaces vicinal to (100) and normal to the [001] pole axis in the fcc structure, the first three miscoordination coefficients are given by (in units of a^{-2})

$$C^{\mathrm{surf}}(1, \Delta\psi) = 8 \cos \Delta\psi + 4 \sin \Delta\psi \qquad (26.31a)$$

$$C^{\mathrm{surf}}(2, \Delta\psi) = 4 \cos \Delta\psi + 4 \sin \Delta\psi \qquad (26.31b)$$

$$C^{\mathrm{surf}}(3, \Delta\psi) = 32 \cos \Delta\psi \qquad (26.31c)$$

assuming $\Delta\psi \leq 26.57°$ for which the (210) plane is reached.

The similarity of these expressions to eq. (26.7b) is rather striking. In fact, in complete analogy with eq. (26.7b), for vicinal surfaces eq. (26.30) may generally be rewritten in terms of the step model as follows:

$$C^{\mathrm{surf}}(\alpha, \Delta\psi) = C^{\mathrm{surf}}_{\mathrm{cusp}}(\alpha) \cos \Delta\psi + [C_{\mathrm{step}}(\alpha)/h] \sin \Delta\psi \qquad (26.32)$$

where $C^{\mathrm{surf}}_{\mathrm{cusp}}(\alpha)$ is the α-th neighbor miscoordination per unit area of the cusped surface (at $\Delta\psi = 0$) while $C_{\mathrm{step}}(\alpha)$ is the α-th neighbor miscoordination per unit length of the steps on the surface.

To quantify the similarity between eqs. (26.32) and (26.7b), we assume that the elastic strain fields surrounding the steps indeed do not cause any broken bonds, an assumption to be validated in section 26.5.2. Both the cusped energy and the line-energy contribution due to the isolated steps in eq. (26.11b) may then be assumed to be proportional to the corresponding miscoordination per unit area. The broken-bond contribution, γ_{b-b}, to the total surface energy may then be written as follows:

$$\gamma_{b-b}(\Delta\psi) \equiv \sum_{\alpha} \beta(\alpha) C^{\mathrm{surf}}(\alpha, \Delta\psi) = \gamma_{\mathrm{cusp}} \cos \Delta\psi + (\Gamma^{s}/h) \sin \Delta\psi \qquad (26.33)$$

with (eq. (26.32))

$$\gamma_{\mathrm{cusp}} \equiv \sum_{\alpha} \beta(\alpha) C^{\mathrm{surf}}_{\mathrm{cusp}}(\alpha) \qquad (26.34)$$

and

$$\Gamma^{s}/h = \sum_{\alpha} \beta(\alpha)\, C_{\mathrm{step}}(\alpha)/h \qquad (26.35)$$

The proportionality constants, $\beta(\alpha)$, are obviously determined by the strengths of the bonds that were broken. In an unrelaxed surface interacting via a pair potential, $\beta(\alpha)$ is identical to the corresponding α-th *nn* perfect-crystal bond energy; by contrast, in a fully relaxed surface $\beta(\alpha)$ obviously represents an average over the slightly varying bond lengths in a given neighbor shell. In contrast to a perfect crystal, in a crystal containing lattice defects the magnitude of $\beta(\alpha)$ may therefore be expected to depend on the local environment of the defects.

Inserting eqs. (26.33) into eq. (26.11b), we obtain

$$\gamma(\Delta\psi) = \gamma_{b-b}(\Delta\psi) + (G^{s-s}_{el}/h^3) \sin^3 \Delta\psi \qquad (26.36)$$

with (eqs. (26.33)–(26.35))

$$\gamma_{b-b}(\Delta\psi) = \cos \Delta\psi \sum_{\alpha} \beta(\alpha) C^{\mathrm{surf}}_{\mathrm{cusp}}(\alpha) + \sin \Delta\psi \sum_{\alpha} \beta(\alpha) C_{\mathrm{step}}(\alpha)/h \qquad (26.37)$$

Similarly, for internal interfaces, if we assume that (i) the elastic strain fields surrounding the dislocations do not create any broken bonds (an assumption also to be validated in section 26.5.2) and (ii) that the line energy in eq. (26.21) is, indeed, dominated by the core term, in analogy to eq. (26.32) we may write:

$$C^{\mathrm{int}}(\alpha, \Delta\psi) = C^{\mathrm{int}}_{\mathrm{cusp}}(\alpha) \cos \Delta\psi + 2[C_{\mathrm{disl}}(\alpha)/b] \sin \Delta\psi \qquad (26.38)$$

where, in analogy to the steps, $C_{\mathrm{disl}}(\alpha)/b$ denotes the α-th *nn* miscoordination per unit length of the interface dislocations while $C^{\mathrm{int}}_{\mathrm{cusp}}(\alpha)$ is the coordination coefficient of the cusped interface. The broken-bond contribution, $\varepsilon_{\mathrm{b-b}}$, to the total interface energy may then be defined as follows:

$$\varepsilon_{\mathrm{b-b}}(\Delta\psi) \equiv \sum_{\alpha} \beta(\alpha) C^{\mathrm{int}}(\alpha, \Delta\psi) = \varepsilon_{\mathrm{cusp}} \cos \Delta\psi + 2(\Lambda'/b) \sin \Delta\psi \tag{26.39}$$

with eq. (26.20b),

$$\varepsilon_{\mathrm{cusp}} \equiv \sum_{\alpha} \beta(\alpha) C^{\mathrm{int}}_{\mathrm{cusp}}(\alpha) \tag{26.40}$$

$$(\Lambda'/b) = \sum_{\alpha} \beta(\alpha) C_{\mathrm{disl}}(\alpha)/b \tag{26.41}$$

Inserting these expressions into eq. (26.20b), in analogy to eq. (26.36) we obtain

$$\varepsilon(\Delta\psi) = \varepsilon_{\mathrm{b-b}}(\Delta\psi) - 2(L^{\mathrm{d-d}}_{\mathrm{el}}/b) \sin \Delta\psi \ln(\sin \Delta\psi) \tag{26.42}$$

with the broken-bond contribution, $\varepsilon_{\mathrm{b-b}}(\Delta\psi)$, given by (compare eq. (26.37))

$$\varepsilon_{\mathrm{b-b}}(\Delta\psi) = \cos \Delta\psi \sum_{\alpha} \beta(\alpha) C^{\mathrm{int}}_{\mathrm{cusp}}(\alpha) + 2 \sin \Delta\psi \sum_{\alpha} \beta(\alpha) C_{\mathrm{disl}}(\alpha)/b \tag{26.43}$$

Equations (26.36) and (26.42) may be inserted into eq. (26.1) to express W^{ad} in terms of its broken-bond (i.e. core) and elastic strain-field contributions, according to (eq. (26.22b))

$$W^{\mathrm{ad}}(\Delta\psi) = W^{\mathrm{ad}}_{\mathrm{b-b}}(\Delta\psi) + 2 \sin \Delta\psi \left[(G^{\mathrm{s-s}}_{\mathrm{el}}/h^3) \sin^2 \Delta\psi + (L^{\mathrm{d-d}}_{\mathrm{el}}/b) \ln(\sin \Delta\psi)\right] \tag{26.44}$$

Here the broken-bond work of adhesion is given by

$$W^{\mathrm{ad}}_{\mathrm{b-b}}(\Delta\psi) = 2\gamma_{\mathrm{b-b}}(\Delta\psi) - \varepsilon_{\mathrm{b-b}}(\Delta\psi) = \sum_{\alpha} \beta(\alpha)[2C^{\mathrm{surf}}(\alpha, \Delta\psi) - C^{\mathrm{int}}(\alpha, \Delta\psi)] \tag{26.45a}$$

or, using eqs. (26.40) and (26.41),

$$W^{\mathrm{ad}}_{\mathrm{b-b}}(\Delta\psi) = \sum_{\alpha} \beta(\alpha)\{[2C^{\mathrm{surf}}_{\mathrm{cusp}}(\alpha) - C^{\mathrm{int}}_{\mathrm{cusp}}(\alpha)] + 2[C_{\mathrm{step}}(\alpha)/h - C_{\mathrm{disl}}(\alpha)/b]\} \tag{26.45b}$$

As noted in the preceding section, the energies of the 'special' and the 'high-angle' interfaces are, by definition, independent of elastic interaction effects. Their work of adhesion is therefore governed completely by the broken-bond contribution in eq. (26.44). For the 'special' interfaces we thus obtain (eq. (26.23))

$$W^{\mathrm{ad}}(\Delta\psi = 0) \equiv W^{\mathrm{ad}}_{\mathrm{b-b}}(\Delta\psi = 0) = (2\gamma_{\mathrm{cusp}} - \varepsilon_{\mathrm{cusp}}) = \sum_{\alpha} \beta(\alpha)[2C^{\mathrm{surf}}_{\mathrm{cusp}}(\alpha) - C^{\mathrm{int}}_{\mathrm{cusp}}(\alpha)] \tag{26.46}$$

while for the 'high-angle' interfaces eq. (26.45b) yields (eq. (26.27))

$$W^{\mathrm{ad}}(\Delta\psi = 90^\circ) = 2 \sum_{\alpha} \beta(\alpha)[C_{\mathrm{step}}(\alpha)/h - C_{\mathrm{disl}}(\alpha)/b] \tag{26.47}$$

These expressions imply that a positive work of adhesion necessitates the dislocation cores in the internal interface to be better coordinated than the cores of the steps in the corresponding two fracture surfaces, i.e. $C_{\mathrm{step}}(\alpha)/h > C_{\mathrm{disl}}(\alpha)/b$. That this is, indeed, the case will be shown in section 26.5 in which the miscoordination per unit length of steps and dislocations will be determined by means of computer simulations.

26.3 COMPUTER SIMULATIONS

As already mentioned, two conceptually different types of interatomic potentials will be used throughout in order to provide some insight into the role of many-body effects. For the fcc metals, results obtained via a semi-empirical embedded-atom-method (EAM) potential fitted to represent Au [12] will be compared with simulations involving the well-known Lennard–Jones (LJ) potential, with only two adjustable parameters, σ and ε, defining the length and energy scales, respectively. Although the LJ potential was fitted

to the lattice parameter and melting point of Cu with ε = 0.167 eV and σ = 2.315 Å, the relative energies of different interfaces are the same for any LJ system if all energies and distances are expressed in units of ε and σ, respectively.

To enable a most direct comparison of free surfaces with GBs, only energies of **symmetrical** tilt boundaries (STGBs) and random grain boundaries (RGBs) will be discussed here. The two fracture surfaces are then identical and, as for the free surfaces, both of these types of GBs are then characterized by only the two DOFs associated with the GB plane, thus permitting a direct investigation of how one particular type of GB edge dislocation is transformed into surface steps.

26.3.1 Energies of free surfaces and GBs

The energies of free surfaces, STGBs and RGBs with a common ⟨110⟩ and ⟨100⟩ pole (or tilt) axis are plotted, respectively, in Figs. 26.4 and 26.5 against the pole (or tilt) angle, $\psi = 2\Delta\psi$ (Fig. 26.1). While these figures show only the EAM results obtained for Au, the LJ potential yields qualitatively identical results.

According to these figures, the energy of the RGB configuration on a given plane is always lower than that of the related two free surfaces. Considering that some of the bonds broken during bulk cleavage fracture are recovered when the two free surfaces are brought back into contact, irrespective of their relative orientation, this result is not surprising. Also, in all instances investigated the STGB configuration on a given plane has a much smaller energy than the RGB on the same plane, with a consequently smaller volume expansion. This difference arises from the local interlocking of the lattice planes in the STGBs, which is possible because of (i) their additional two translational DOFs, (T_x, T_y), parallel to the GB, and (ii) their very small planar unit cells (with only one atom per (*hkl*) plane, as in the perfect crystal [20]). We note that, because the STGB configuration on the (100) and (110) plane is identical to the perfect crystal [20], the corresponding STGB energies vanish. Also, although finite, the energy of the STGB on the (111) plane (the so-called (111) twin boundary), is very small for both potentials (Table 26.1). A realistic comparison of the relative energies of STGBs, RGBs and free surfaces should therefore involve the less-dense planes.

We should mention that the Au(EAM) energies are substantially lower than the measured **average** surface energy of about 1500 mJ/m² of gold [21]. Similarly large (~60–80%) discrepancies between

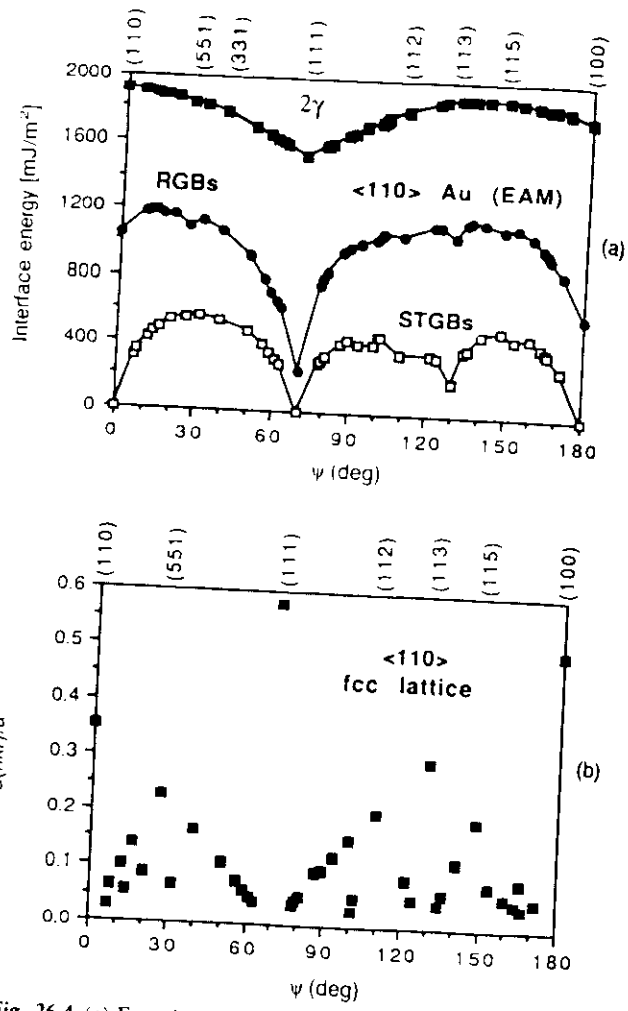

Fig. 26.4 (a) Energies (in units of mJ/m²) of fully relaxed free surfaces (2γ), STGBs and RGBs on planes perpendicular to the ⟨110⟩ pole axes for the Au(EAM) potential. $\psi = 2\Delta\psi$ is the tilt rotation angle about ⟨110⟩ (see also Fig. 26.1). The lines connecting the data points are merely a guide to the eye. (b) Related interplanar lattice spacings, $d(hkl)$, in units of the lattice parameter a.

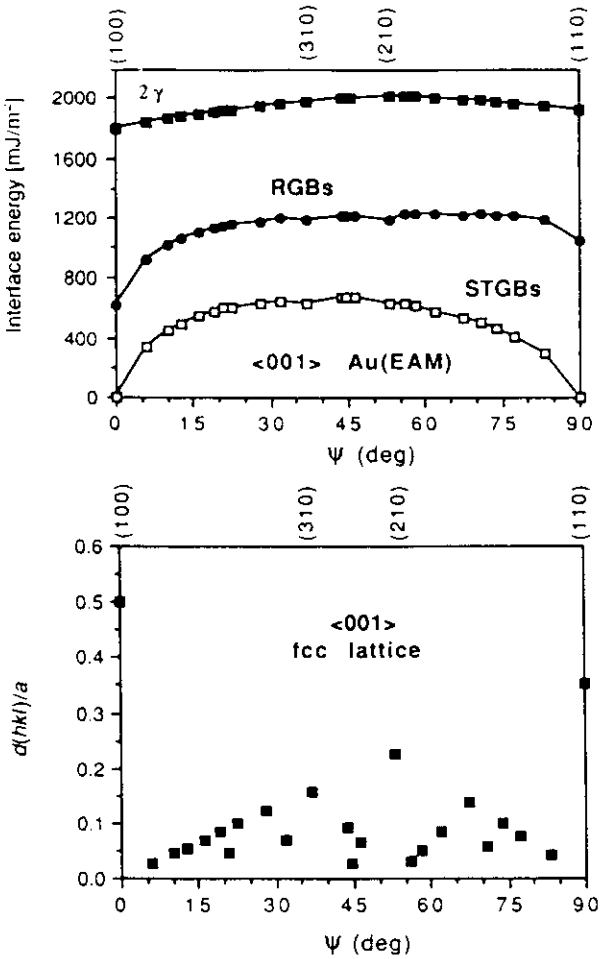

Fig. 26.5 Same as Fig. 26.4, but for interface planes perpendicular to ⟨001⟩.

computed and measured surface energies are also found for other fcc metals [12]. As already mentioned, we nevertheless hope that a comparison of relative energies of surfaces and GBs which uses these potentials is meaningful.

A comparison of the energies in Figs. 26.4(a) and 26.5(a) with the interplanar spacings, $d(hkl)$, shown in Figs. 26.4(b) and 26.5(b) (see also Table 26.2) demonstrates that the appearance of cusps in the energies of free surfaces, RGBs and STGBs is closely connected with relatively large values of the interplanar spacings $d(hkl)$. In contrast with the free surfaces, however, which show only the three cusps associated with the three densest planes, the GBs show minor cusps all the way up to about the 10th- or 11th-densest fcc plane. (Notice, however, that in the case of the STGBs, the (100) and (110) interplanar spacings are irrelevant because the STGBs on these planes are identical to the perfect crystal ([20].) As a consequence, the energies of the free surfaces vary much more smoothly as a function of the pole angle ψ. This difference between GBs and free surfaces is thought to be due to the absence of the three translational DOFs in the latter. In STGBs, by contrast, the possible rigid-body translations in **T** enable a much more effective minimization of the GB energy, particularly for GBs with the smallest planar unit cells, i.e. those on planes with the largest $d(hkl)$ values, which consequently give rise to energy cusps. With only one translational DOF (that associated with volume expansion at the GB), RGBs fall somewhere

Table 26.1 Comparison of the surface energies, γ, and nearest-neighbor coordination coefficients, $C(1)/a^2$ (see eq. (26.29)) obtained for the two potentials for surface normals in the four principal cubic directions [19]. For comparison, the corresponding energies and coordination coefficients of STGBs [23] and RGBs [9] are also listed. All energies are in units of mJ/m^2 (=erg/cm^2)

	(hkl)	γ	$C(1)/a^2$	ε^{RGB}	$C(1)/a^2$	ε^{STGB}	$C(1)/a^2$
Cu(LJ)	(111)	839	6.93	432	3.17	2	0
Au(EAM)	(111)	767	6.93	249	1.80	2	0
Cu(LJ)	(100)	892	8.00	810	7.90	0	0
Au(EAM)	(100)	897	8.00	616	6.30	0	0
Cu(LJ)	(110)	957	8.48	1329	12.76	0	0
Au(EAM)	(110)	957	8.48	1041	11.43	0	0
Cu(LJ)	(113)	961	8.44	1431	13.73	293	2.41
Au(EAM)	(113)	944	8.44	1069	9.46	211	2.41

Table 26.2 Interplanar spacing, $d\,hkl$, in units of the lattice parameter a, for the 11 most widely spaced planes in the fcc lattice. These planes also correspond to the ones with the highest planar density of atoms, i.e. the smallest planar repeat unit cells

No.	*hkl*	$d\,hkl\,/a$
1	111	0.5774
2	100	0.5000
3	110	0.3535
4	113	0.3015
5	331	0.2294
6	210	0.2236
7	112	0.2041
8	115	0.1925
9	513	0.1690
10	221	0.1667
11	310	0.1581

between STGBs and free surfaces as far as their sensitivity towards rigid-body translations is concerned, with a consequently more smoothly varying energy plot than that of the STGBs. (For a quantitative analysis of the role of the interplanar spacing in the above energies, see section 26.3.3.)

That the energies in Figs. 26.4(a) and 26.5(a) are intimately connected with the number of nearest-neighbor bonds per unit area broken upon creation of the free surface or GB, $C(1)$ (see eq. (26.29)), is demonstrated in Table 26.1. It is interesting to note that in the case of the free surfaces, the coordination coefficients extracted from the simulations were the same for both the unrelaxed and fully relaxed structures and for both potentials. As discussed further in section 26.5, this suggests that the elastic strain fields surrounding the surface steps do not cause any broken bonds in the sense defined above; instead, similar to the case of dislocations, all broken bonds arise from the highly disordered **cores** of the steps. We note, however, that by choosing the primitive planar unit cell of the free surface, reconstruction was systematically discouraged in our simulations. If reconstruction were to take place, one would in principle expect differences in the average atom coordination between the unrelaxed and relaxed structures.

As discussed in section 26.2.4, for the 'high-angle' free surfaces and GBs, i.e. those well outside

Table 26.3 Core energies of steps and edge dislocations in STGBs and RGBs in fcc metals extracted from the simulation results in the 'high-angle' limit via eqs. (26.26) or (26.27); see also Figs. 26.6(a) and (b) and Fig. 26.8

From	*STGBs* $\Lambda_{\mathrm{core}}/b\,/\,\Gamma_{\mathrm{core}}/b$		*RGBs* $\Lambda_{\mathrm{core}}/b\,/\,\Gamma_{\mathrm{core}}/b$	
	$\varepsilon_{\mathrm{core}}/2\gamma_{\mathrm{core}}$	$W^{\mathrm{rel}}_{\mathrm{sep}}/2\gamma_{\mathrm{core}}$	$\varepsilon_{\mathrm{core}}/2\gamma_{\mathrm{core}}$	$W^{\mathrm{rel}}_{\mathrm{sep}}/2\gamma_{\mathrm{core}}$
Cu LJ	0.48	0.48	0.85	0.86
Au EAM	0.33	0.33	0.60	0.62

of any cusps in which the cores overlap completely, one would expect a linear relationship between the free-surface and GB energies [see eqs. (26.24)–(24.26)]. To investigate this relationship, in Figs. 26.6(a) and (b) the energies of STGBs and RGBs are plotted against 2γ. As expected, the energies associated with vicinal orientations scatter widely but, as indicated by the dashed lines, are systematically related to the energies of the densest (cusped) planes. As shown in the inserts, however, for all the remaining ('high-angle') interfaces a reasonably good correlation exists between the energies of STGBs and RGBs, on the one hand, and the energy of free surfaces, on the other. According to eq. (26.26), the slopes of the solid lines through the origin give the ratio, $f_c \equiv \varepsilon_{\mathrm{core}}/2\gamma_{\mathrm{core}}$, of the core energies of steps and dislocations. According to the values listed in Table 26.3, this ratio is less than one in all cases, consistent with the positive work of adhesion of the internal interfaces (see below). As discussed further in section 26.4, the origin of the qualitatively different behavior of the 'special' and 'vicinal' interfaces in Fig. 26.6 compared to the 'high-angle' interfaces lies in the fundamental difference between the short-ranged elastic strain fields near the steps, which are contrasted by the long-ranged strain fields near the dislocations.

26.3.2 Cleavage-fracture energies

The above simulation data for free surfaces and GBs may be combined to determine the work of adhesion for the internal interfaces. The plots thus

STGB energy [mJ/m^2]

RGB energy [mJ/m^2]

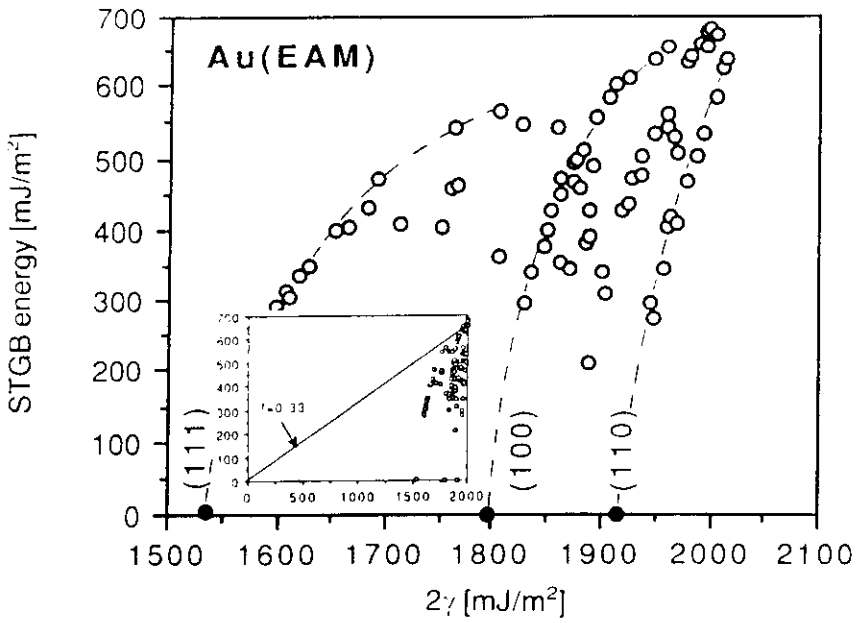

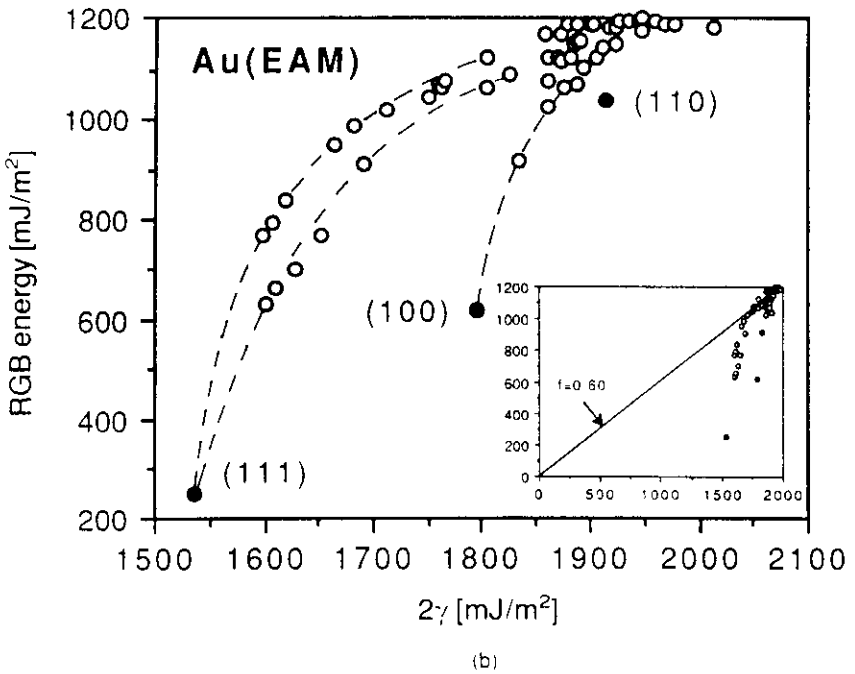

Fig. 26.6 Energies of (a) STGBs and (b) RGBs plotted against the bulk-cleavage energy, 2γ (in mJ/m^2) in the fcc lattice. Dashed lines correlate 'vicinal' orientations with their corresponding 'cusped' orientations (solid symbols). The two sets of (111) vicinals correspond to tilting toward (100) and (110) surfaces respectively. The solid lines in the inserts show a fit to the energies of the 'high-angle' interfaces (i.e. those far from any of the cusps) through the origin (eqs. (26.24)–(26.26)). The slopes, f_s, obtained for the two potentials are listed in Table 26.3.

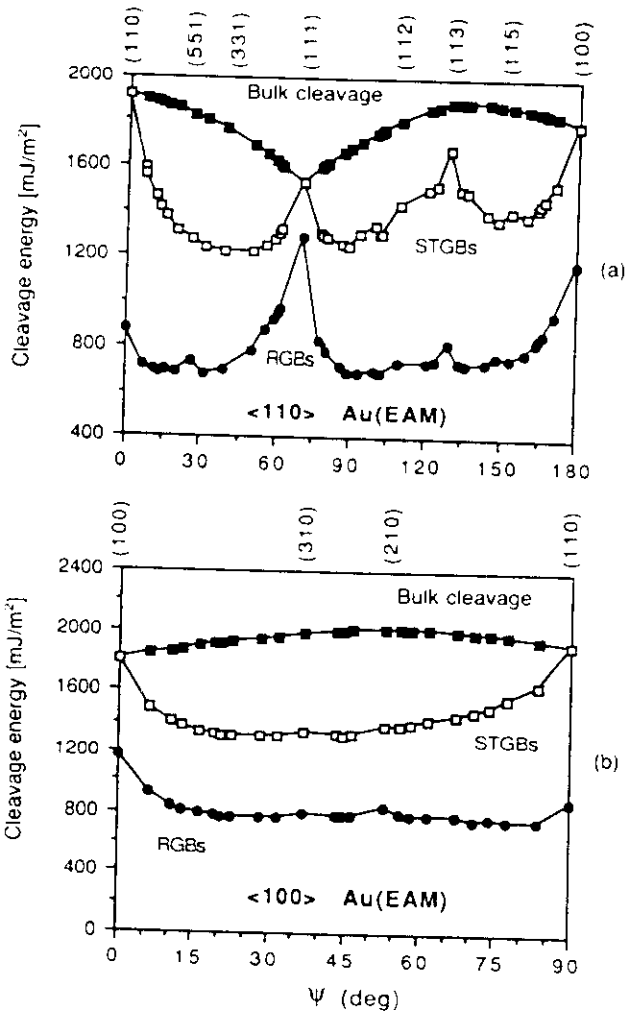

Fig. 26.7 Cleavage energies for the STGBs in Figs. 26.4(a) and 26.5(a). For comparison, the bulk ideal-crystal cleavage energies ($= 2\gamma$) are also shown.

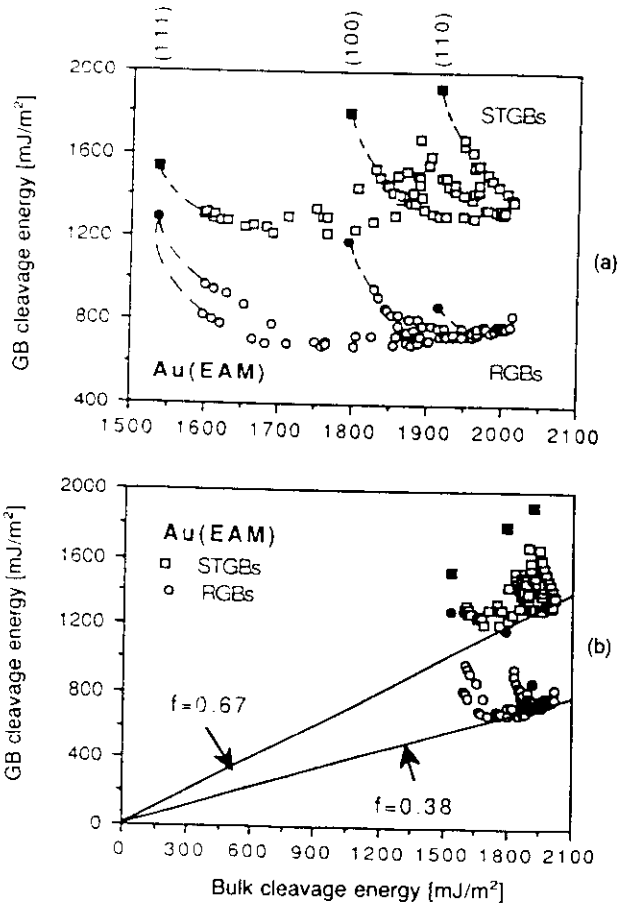

Fig. 26.8 Plots analogous to Figs. 26.6(a) and (b) showing (a) the cleavage energies of the STGBs and the RGBs plotted against the bulk-cleavage energy, 2γ (in mJ/m^2). Solid symbols mark the cusped orientations and the dashed lines connect corresponding vicinal orientations. The two sets of (111) vicinals correspond to tilting toward (100) and (110) surfaces respectively (Fig. 26.7(a)). The solid lines in the blow-up in (b) show a fit to the cleavage energies of the 'high-angle' interfaces through the origin. According to eq. (26.28), their work of adhesion is proportional to the energy of the related two fracture surfaces. For both potentials, values of $f_c = 1 - f_{ad}$ as obtained from the slopes, f_{ad}, are also listed in Table 26.3.

obtained from Figs. 26.4(a) and 26.5(a) are shown in Figs. 26.7(a) and (b), respectively. A comparison of the STGB and RGB data shows qualitatively the same behavior for both types of GBs. This similarity is particularly remarkable in the vicinity of the (100) and (110) planes for which, in both lattices, the STGB energy vanishes identically while the RGB energy remains finite. From these figures, the correlation between a large value of $d(hkl)$ and a **large** work of adhesion is rather apparent, as is the correlation between large $d(hkl)$ values and **small** values of 2γ.

This correlation between the **cusps** in the bulk ideal-crystal cleavage energy, $E^{cl} = 2\gamma$, and the **peaks** in the GB work of adhesion, W^{ad}, is particularly interesting. Intuitively one would expect the opposite behavior: if the corresponding free-

surface energy is particularly small one would think that it should be easier to separate a particular bicrystal. However, a comparison of the corresponding interface energies in Figs. 26.4(a) and 26.5(a) shows that while 2γ may be small for a given cusp orientation, the corresponding GB energy is significantly smaller still. Since the energetics of the interfaces at cusped orientations are dominated by miscoordination (section 26.2.5), the origin of this behavior is largely crystallographic (section 26.5.2). Furthermore, the elastic-interaction energy and the high miscoordination of the dislocations in GBs results in a more rapid increase in the GB energies, as compared to free-surface energies. This leads to relatively higher GB energies, and correspondingly smaller works of adhesion, for the high-angle orientations.

To enable a more quantitative analysis of the relationship between the bulk ideal-crystal cleavage energy, E^{cl}, and the GB work of adhesions, W^{ad}, Fig. 26.8 shows the two plotted against one another. These figures suggest the distinction of two types of GBs as far as their work of adhesion is concerned. First, for the 'special' GBs and their vicinals, W^{ad} **decreases** with increasing E^{cl}. This behavior is due to the elastic energy of the vicinals. Second, for all remaining GBs (i.e. those that are neither 'special' nor 'vicinal'), W^{ad} **increases** with increasing E^{cl}, as seen from Figs. 26.8(a) and (b).

26.3.3 Role of the interplanar lattice spacing: vicinal versus special interfaces

The simulation results presented in the preceding suggest a special role of the densest planes in the energies of free surfaces, STGBs and RGBs, and therefore in the work of adhesion. Since both the STGBs and the symmetrical RGBs are fully characterized macroscopically by only the two DOFs associated with the GB normal, a comparison of their energies with those of free surfaces enables a systematic investigation of the role of the interface **plane** in both their energy and work of adhesion.

To analyze the role of the interface plane quantitatively, in Figs. 26.9(a) and (b) the energies of the free surfaces and GBs are plotted against

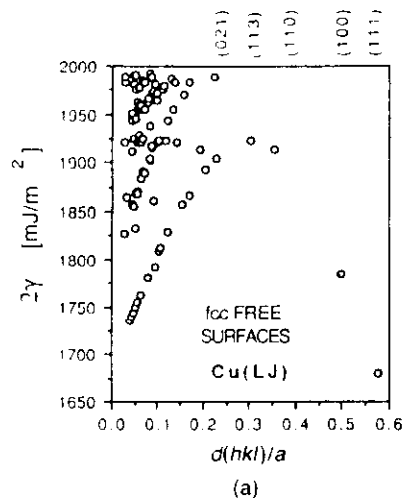

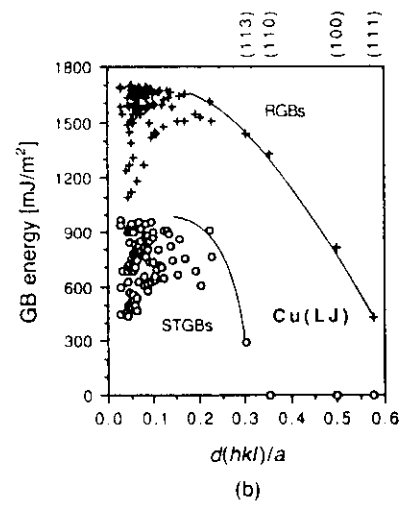

Fig. 26.9 Energies (in mJ/m^2) of fully relaxed (a) free surfaces (2γ) and (b) STGBs and RGBs plotted against $d(hkl)/a$. The densest surface planes (Table 26.2) are indicated on the top.

$d(hkl)$. These plots demonstrate that the criterion that a large interplanar spacing gives rise to a particularly low GB energy is valid only for the few densest lattice planes, i.e. for the 'special' interfaces giving rise to the cusps. For the smaller values of $d(hkl)$ the simulation data scatter widely, indicating that the GB energy is not governed by the interplanar spacing exclusively.

That the energies of the **vicinal** interfaces *cannot* be governed by $d(hkl)$ becomes obvious if we

consider, for example, the free surfaces and GBs in the vicinity of the cusps in Figs. 26.4(a) and 26.5(a). Their energies are obviously governed by the energy and interplanar spacing of the free surface or GB at the bottom of the related cusp. As a cusp is approached, the corresponding value of $d(hkl)$ approaches zero (Figs 26.4(b) and 26.5(b)). Then, at the cusp, the interplanar spacing suddenly jumps to a finite and large value associated with the cusp. For example, the (41, 41, 42) plane is very close to the (111) plane, however with a practically vanishing value of $d(hkl)$, because the latter is proportional to $(h^2 + k^2 + l^2)^{-1/2}$. The energies of the free surface, the STGB and the RGB on the (41, 41, 42) plane of the fcc lattice are therefore practically the same as those on the (111) plane. Consequently, while the energy decreases smoothly towards that of the cusped orientation, $d(hkl)$ does not vary steadily as a function of ψ, which is the reason for the absence of a direct relation between the two for the vicinal but not the cusped interface-plane orientations.

A detailed analysis of the distribution of all the data points in Figs. 26.9(a) and (b) confirms that for every plane with a relatively high $d(hkl)$ value, there is a point at $d(hkl) = 0$ (associated with some infinitesimally close vicinal interface) with identical energy. All other surfaces associated with the same cusp then fall on a smooth line emanating from this point as $d(hkl)$ increases slowly from zero.

As is well known, the distinction between vicinal and special interfaces is very useful for describing the underlying atomic structure of surfaces and GBs. For the case of the STGBs, Weins *et al.* [24] demonstrated 20 years ago that the structure of those STGBs in the vicinity of a major cusp may be decomposed into the polyhedral units of, and the angular deviation from, the 'special' STGB at the bottom of that cusp. (These structural units correspond to the dislocation cores in the Read–Shockley model considered in section 26.2.2.) By comparison, for the case of free surfaces it has been known for well over half a century that the structure and energy of 'vicinal' surface orientations is governed by the number of and distance between the steps introduced into the nearby 'flat'

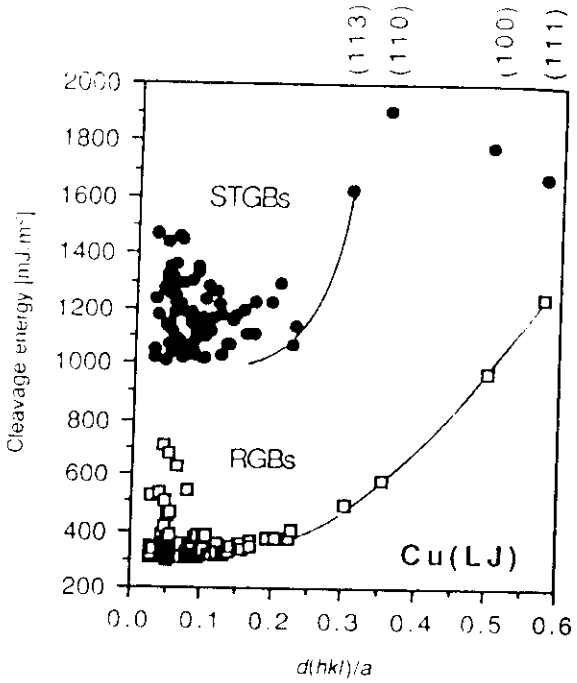

Fig. 26.10 Work of adhesion (in mJ/m^2) of fully relaxed STGBs and RGBs in fcc metals against $d(hkl)/a$ (see also Table 26.4).

(i.e. step-free) principal surface (section 26.2.1) [6].

Finally, by subtracting corresponding data points in Figs. 26.9(a) and (b), the role of $d(hkl)$ in the work of adhesion is readily analyzed (Fig. 26.10). As expected, the distinction between **vicinal** and **special** GB-plane orientations is the same in the cleavage energies as that discussed above for the underlying GB and free-surface energies. It is interesting to note, however, that the particularly **low** energy of both the free surfaces and GBs on the densest planes is accompanied by a particularly **high** work of adhesion. This counter-intuitive behavior of the special interface planes is due to the very low degree of miscoordination at the special GB interfaces (section 26.5). While therefore the interplanar spacing of the lattice planes parallel to the interface should be of importance only for the cusped orientations, it is obviously irrelevant for vicinal ones.

In summary, it appears that in assessing the role

Table 26.4 Work of adhesion (see eq. (26.1)) for STGBs and RGBs for the four densest planes of the fcc lattice obtained from Table 26.1 in units of mJ/m^2. For comparison, the bulk ideal-crystal cleavage-fracture energy ($= 2\gamma$) is also listed

hkl	*Cu(EAM)*			*Au(EAM)*		
	STGBs	*RGBs*	*bulk* (2γ)	*STGBs*	*RGBs*	*bulk* (2γ)
⟨111⟩	1676	1246	1678	1532	1287	1534
⟨100⟩	1784	974	1784	1794	1178	1794
⟨110⟩	1914	585	1914	1914	873	1914
⟨113⟩	1629	491	1922	1677	819	1888

of the GB plane in the energies of free surfaces, STGBs and RGBs, and therefore in the work of adhesion, one should distinguish between 'special' and 'vicinal' interface planes. While the energies of the **special** interfaces are governed by the interplanar spacing of the lattice planes parallel to the interface plane, the value of $d(hkl)$ is irrelevant for the **vicinal** ones. Plots such as Figs. 26.9 and 26.10 provide a quick and simple method for separating the two types of interfaces for a given crystal structure and interatomic potential used in the simulations.

26.4 CORE AND ELASTIC STRAIN-FIELD EFFECTS IN FREE SURFACES AND GBs

We are now ready to test some of the assumptions made in sections 26.2.1 and 26.2.2 concerning the core energies of and elastic interactions between steps, on the one hand, and dislocations, on the other. For that purpose, the energies of free surfaces and STGBs perpendicular to ⟨100⟩ determined for the Au(EAM) potential (Fig. 26.5(a)) will be analyzed in some detail.

26.4.1 Surface steps

We first consider the line energies of surface steps. According to Fig. 26.5(a), two cusped orientations, associated with the (100) and (110) surfaces, are encountered when rotating about a ⟨001⟩ pole axis. For a detailed investigation of the line energies of the corresponding steps, a number of surfaces in the close vicinity of these cusps were simulated in addition to those shown in Fig. 26.5(a). For reasons to become evident below, these most vicinal surfaces are needed for a reliable determination of the line energies of isolated steps, i.e. in the limit for $\delta \to \infty$. According to Table 26.5, the largest separation considered for the (100) steps is $\delta = 21.54a$, by comparison with $\delta = 15.95a$ for the (110) step. By investigating step separations down to about $1.12a$ (Table 26.5), we hope to gain insight into the nature of the elastic interaction between the steps as a function of their distance.

The relaxed and unrelaxed energies of all surfaces perpendicular to ⟨001⟩ considered here are shown in Fig. 26.11. We note that both sets of energies are plotted against $\Delta\psi_1$, the angular

Table 26.5 Geometrical parameters associated with the steps considered in detail in this section. n is the step height, while a denotes the lattice parameter.

n	*Pole axis*	*Plane*	*h/a*	$\Delta\psi_0$ *[deg]*	*Vicinal plane*	*δ/a*	*Vicinal plane*	*δ/a*
1	⟨100⟩	(100)	0.5000	0.00–26.56	(043 1)	21.54	(021)	1.12
2	⟨100⟩	(100)	0.3535	0.00–18.44	(023 22)	15.95	(021)	1.12

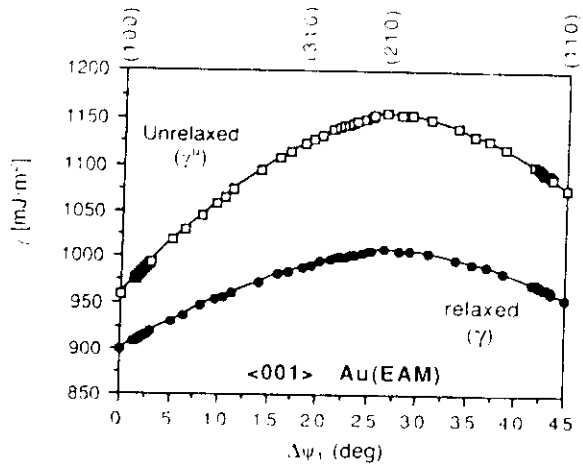

Fig. 26.11 Unrelaxed (γ^u) and relaxed (γ) energies of free surfaces of Au perpendicular to (001) against $\Delta\psi_1$, with $\Delta\psi_2 = 45° - \Delta\psi_1$. Notice that by comparison to Fig. 26.5(a), considerably more vicinal surfaces close to the (100) and (110) planes are considered here (Table 26.5). Notice that $\Delta\psi_1 = \psi/2$.

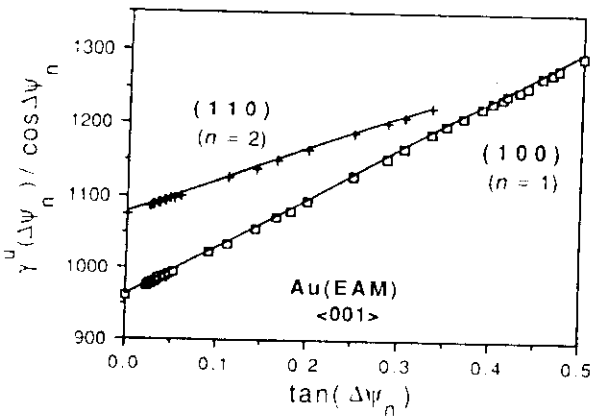

Fig. 26.12 Unrelaxed energies of Fig. 26.11, $\gamma^u/\cos\Delta\psi$ (in mJ/m^2), plotted against $\tan\Delta\psi$ (eq. (26.48)) for the (100) and (110) vicinals perpendicular to (001). The line energies of the unrelaxed steps extracted from the slopes of the solid lines are listed in Table 26.6.

deviation from the (100) cusp. The results associated with the (110) cusp should actually be plotted against, and will be interpreted in terms of the angle $\Delta\psi_2 = 45° - \Delta\psi_1$.

To determine the line energy of the isolated steps, it is useful to first consider the unrelaxed surface energy, γ^u. Without relaxation, elastic strain fields cannot develop near the steps; γ^u is therefore governed completely by core effects (i.e. broken bonds), according to (eqs. (26.11b) and (26.12)):

$$\gamma^u(\Delta\psi) = \gamma^u_{cusp}\cos\Delta\psi + (\Gamma^u_{core}/h)\sin\Delta\psi \tag{26.48}$$

where γ^u_{cusp} denotes the unrelaxed energy of the cusped surface, while Γ^u_{core} is the unrelaxed core energy per unit length of the steps. To test the validity of eq. (26.48), in Fig. 26.12 the values of $\gamma^u(\Delta\psi)/\cos\Delta\psi$ obtained from Fig. 26.11 are plotted against $\tan\Delta\psi$. The extremely good linearity exhibited in Fig. 26.12 is proof that, down to the smallest values of δ, the unrelaxed energy is determined by a δ-independent core energy of the steps and, hence, by the number of broken bonds per unit surface area (eqs. (26.32) and (26.37)). The unrelaxed core energies obtained from the related slopes are listed in Table 26.6.

Next, in order to focus entirely on the elastic contribution to the line energy, it is useful to define the (positive) relaxation energy (eqs. (26.11b) and (26.48)),

$$\begin{aligned}\Delta\gamma(\Delta\psi) &\equiv \gamma^u(\Delta\psi) - \gamma(\Delta\psi)\\ &= (\gamma^u_{cusp} - \gamma_{cusp})\cos\Delta\psi\\ &\quad + [(\Gamma^u_{core} - \Gamma^\infty)/h]\sin\Delta\psi\\ &\quad - (G^{s-s}_{el}/h^3)\sin^3\Delta\psi\end{aligned} \tag{26.49}$$

where, according to eq. (26.12), the relaxed line energy of the isolated steps, Γ^∞, contains contributions from both the relaxed cores and elastic strain fields; therefore

$$\Gamma^u_{core} - \Gamma^\infty = \Gamma^u_{core} - \Gamma^\infty_{core} - \Gamma^\infty_{el} \tag{26.50}$$

Using the data in Fig. 26.11, the relaxation energies shown in Fig. 26.13 are readily obtained. In this representation of the simulation data, the discontinuity in the slope at the (210) plane delimiting the two cusps is particularly noticeable (Table 26.5).

To extract the step-step interaction energy from the data in Fig. 26.13 by means of eq. (26.49), we take advantage of the fact that for a large separation between the steps (i.e. for the smallest values of $\Delta\psi$), their interaction energy in the third term on the right-hand side of eq. (26.49) should be

Table 26.6 Step parameters determined for the Au (EAM) potential (in units of mJ/m²)

Pole axis	Cusped plane	Height (h/a)	γ^{u}_{cusp}	γ_{cusp}	Γ^{u}_{core}/h	$(\Gamma^{u}_{core} - \Gamma^{\infty})/h$	Γ^{∞}/h	$(G^{s-s}_{el}\gamma/h^3)$	$(G^{s-s}_{n}\gamma/h^3)$
(100)	(100)	0.5	960.6	898.6	669.5 ± 0.5	265.4 ± 0.5	404.1 ± 1.0	570 ± 60	280 ± 10
(100)	(100)	0.3535	1077.0	958.5	431.4 ± 0.5	144.7 ± 0.5	286.7 ± 1.0	540 ± 50	280 ± 10

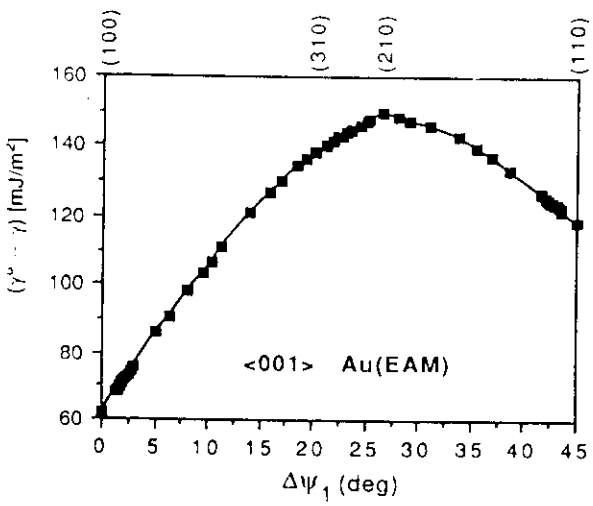

Fig. 26.13 Relaxation energies, $\Delta\gamma = \gamma^{u} - \gamma$ (eq. (26.49)), for the free surfaces of Fig. 26.11. The discontinuity in the slope at the (210) orientation, delimiting the two cusps at $\Delta\psi_1 = 0°$ and 45°, respectively, is clearly visible.

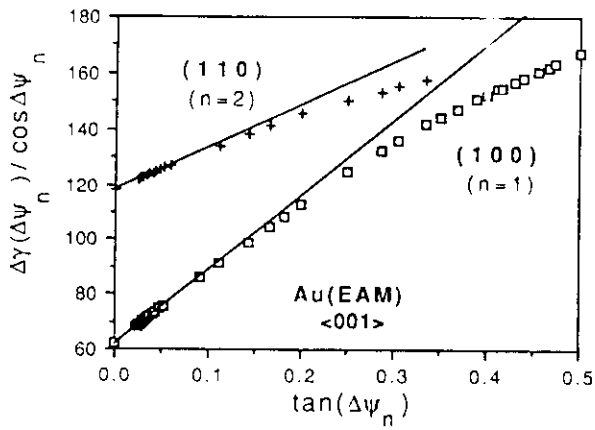

Fig. 26.14 Relaxation energies of Fig. 26.13 plotted against $\tan\Delta\psi$ (eq. (26.49)). From the slopes of the straight-line fits to the **low-angle** data (solid lines), the line energies of the isolated, non-interacting steps can be extracted; these are listed in Table 26.6.

negligibly small compared to the line-energy contribution in the second term (eqs. (26.10) and (26.15)). Similar to Fig. 26.12 we therefore plot $\Delta\gamma(\Delta\psi)/\cos\Delta\psi$ against $\tan\Delta\psi$ (Fig. 26.14); the slope of a straight-line fit to the low-angle data in Fig. 26.14 (indicated in the figure), should therefore yield the line energies of the isolated, non-interacting steps. According to Fig. 26.14, for values of $\tan\Delta\psi$ less than about 0.05, these plots are, indeed, very well represented by straight lines. Their slopes $(\Gamma^{u}_{core} - \Gamma^{\infty})/h$, obtained from a linear fit through the origin for only the few most vicinal surfaces are listed in Table 26.6. The convergence of these fits was tested by including variable numbers of the closest few vicinals in the fit, with no discernible change in the slope, confirming that the largest separations between steps considered here (Table 26.5) are, indeed, large enough to enable a reliable determination of the line energies of non-interacting steps.

Finally, if we attribute any deviations from the straight lines in Fig. 26.14 to the elastic interaction between the steps, i.e. if we plot the difference (eq. (26.49))

$$\begin{aligned}\gamma^{s-s}_{el}(\Delta\psi)/\cos\Delta\psi &\equiv -\Delta\gamma(\Delta\psi)/\cos\Delta\psi + (\gamma^{u}_{cusp} - \gamma_{cusp}) \\ &\quad + [(\Gamma^{u}_{core} - \Gamma^{\infty})/h]\tan\Delta\psi \\ &\overset{?}{=} (G^{s-s}_{el}/h^3)\sin^2\Delta\psi\tan\Delta\psi \qquad (26.51)\end{aligned}$$

against $\sin^2\Delta\psi\tan\Delta\psi$, we expect a straight line with a slope of G^{s-s}_{el}/h^3 if the interaction is, indeed, proportional to $1/\delta^2$ (eqs. (26.10) and (26.15)) [16]. According to Figs. 26.15(a) and 26.16(a), a reasonably good linear behavior is, indeed, obtained for the surfaces with the largest separations between the steps (typically $\delta \leq 10a$ for the (100) vicinals, and $\delta \leq 7a$ for the (110) vicinals). The

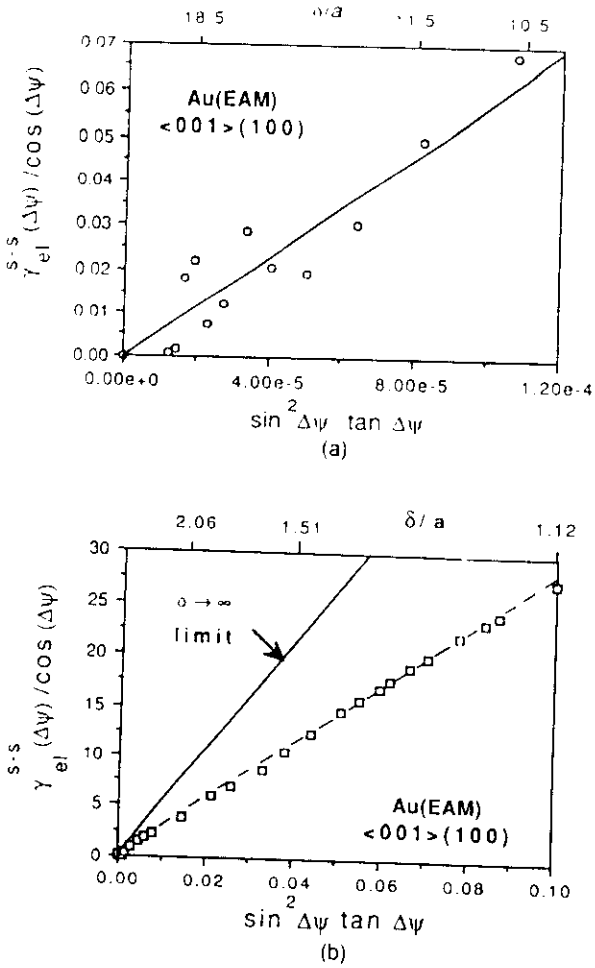

Fig. 26.15 Step–step-interaction contribution to the surface energy, $\gamma_{el}^{s-s}(\Delta\psi)/\cos\Delta\psi$ (eq. (26.51)) for (a) the largest and (b) the smallest values of δ (indicated on the top) for the (100) vicinals plotted against $\sin^2\Delta\psi \tan\Delta\psi$ (in mJ/m^2). The slope of the solid line in (a), G_{el}^{s-s}/h^3, obtained from a least-squares fit through the origin (eq. (26.51)), is listed in Table 26.6 together with the slope of the dashed line, G_{n-1}^{s-s}/h^3, which represents a least-squares fit to the small-δ data alone.

slopes of the solid lines, obtained from a least-squares fit through the origin, are listed in Table 26.6. This $1/\delta^2$ variation of the step–step interaction energy in Au is in good agreement with recent simulations for Si [25] in which the same behavior was found for both steps on a flat surface and vicinal surfaces.

Not too surprisingly, for smaller step separations significant deviations from this linear behavior are apparent: As illustrated in Figs. 26.15(b) and 26.16(b), the step–step repulsion does not increase as rapidly with decreasing δ (indicated in the tops of these figures) as predicted by the Marchenko–Parshin formula (eqs. (26.10), (26.15), and (26.51)). That the step–step repulsion *cannot* increase indefinitely is intuitively obvious because the perfect-crystal-like regions mediating this elastic interaction are virtually eliminated when the step cores start to overlap. Another reason for the failure of eq. (26.49) for small values of δ can be expected to arise from a δ-dependence of the relaxed core energy, Γ_{core}, as the cores start to interact.

Because no theoretical predictions are available for the required modification, at small separations, of either the elastic step–step interaction or the core energy, at present the two effects causing deviations from eq. (26.11(b)) cannot be separated. It appears, however, that Figs. 26.15(b) and 26.16(b) provide a clue. As is evident from these figures, even for the smallest separations between the steps their interaction energy varies linearly with $1/\delta^2$ (see the dashed lines in the figures). By comparison with the large-δ Marchenko–Parshin limit, however (derived from isotropic linear continuum-elasticity theory; see the solid lines in these figures), the slopes of the dashed lines, labeled (G_{n-1}^{s-s}/h^3), are smaller by about a factor of two (Table 26.6).

Two interpretations of the observed small-δ behavior appear possible. First, linear continuum elasticity theory used to derive the Marchenko–Parshin expression in eq. (26.10) obviously breaks down when the steps get too close. Although a non-linear-elastic extension of eq. (26.8) is not available, the above results would suggest that the non-linear effects give rise to a reduced prefactor, G_{n-1}^{s-s}, without affecting the basic functional form of the Marchenko–Parshin formula.

Second, as the steps get rather close, one could envision a modification of the core energies of the steps, i.e. a non-elastic core–core interaction. Such an interaction – which, according to the above results, would be attractive – could be incorporated

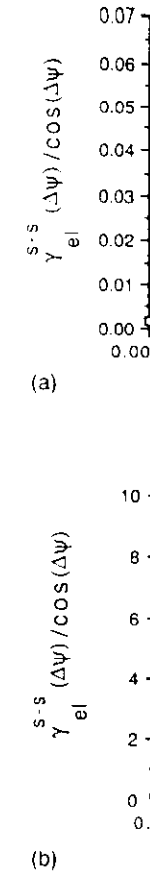

Fig. 26.16 Sa
squares-fit par
Table 26.6.

into the th
line energy

$\Gamma(\delta) = \Gamma$

Analogous
core–core i

$\Gamma_{core}(\delta) =$

and eq. (26

$\gamma(\Delta\psi) -$
$+ (G_{el}^{s}$

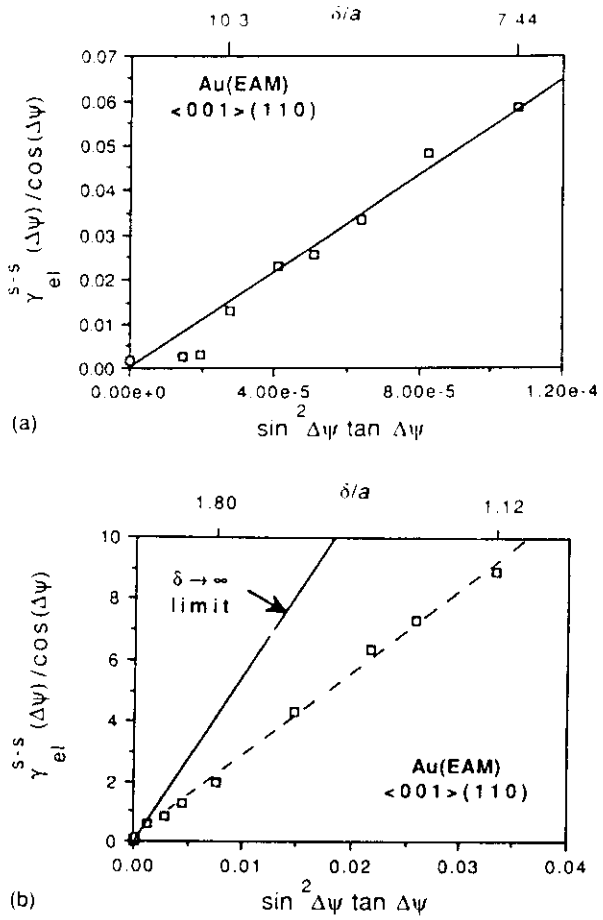

Fig. 26.16 Same as Fig. 26.15 for the (110) vicinals. The least-squares-fit parameters of the solid and dashed lines are listed in Table 26.6.

into the theory of section 26.2.1 by replacing the line energy in eq. (26.8) by

$$\Gamma(\delta) = \Gamma_{core}(\delta) + \Gamma_{el}(\delta) \tag{26.52}$$

Analogous to eq. (26.9), one can then define the core–core interaction energy, $\Gamma_{core}^{s-s}(\delta)$, as follows:

$$\Gamma_{core}(\delta) = \Gamma_{core}^{\infty} + \Gamma_{core}^{s-s}(\delta) \tag{26.53}$$

and eq. (26.11b) becomes instead:

$$\gamma(\Delta\psi) - \gamma_{cusp}\cos\Delta\psi = (\Gamma^{\infty}/h)\sin\Delta\psi + (G_{el}^{s-s}/h^3)\sin^3\Delta\psi = [\Gamma_{core}^{s-s}(\delta)/h]\sin\Delta\psi \tag{26.54}$$

If one were to assume the Marchenko–Parshin contribution to remain unchanged even at the smaller separations, $\Gamma_{core}^{s-s}(\delta)$ could readily be extracted from the simulation data in Figs. 26.15(b) and 26.16(b) by subtracting the data points from the corresponding solid lines. The attractive core–core interaction energies thus obtained would obviously still follow a $1/\delta^2$ dependence. However, to understand – or at least rationalize – this result seems difficult.

To summarize and, in particular, to elucidate the overall magnitude of the step–step interaction relative to the other contributions to the surface energy, we return to the original expression for γ in eq. (26.11b), which may more generally be rewritten as follows:

$$\gamma(\Delta\psi) = \gamma_{cusp}\cos\Delta\psi + \gamma^{\infty}(\Delta\psi) + \gamma^{s-s}(\Delta\psi) \tag{26.55}$$

Here the contribution due to the total line energy of non-interacting steps is given by (eq. (26.11b))

$$\gamma^{\infty}(\Delta\psi) = (\Gamma^{\infty}/h)\sin\Delta\psi \tag{26.56}$$

while, for the present purpose, no particular functional form needs to be assumed for the (elastic or non-elastic) contribution, $\gamma^{s-s}(\Delta\psi)$, due to the step–step interaction. Using the values of γ_{cusp} and (Γ^{∞}/h) listed in Table 26.6 together with the simulation data in Figs. 26.15(b) and 26.16(b), the three contributions to γ in eq. (26.55) may be plotted separately against $\Delta\psi_1$ for both types of steps (Fig. 26.17).

Figure 26.17 demonstrates that the overall surface energy is dominated by the energies, $\gamma_{cusp}\cos\Delta\psi$, of the cusped orientations projected onto the vicinal planes. For both types of steps, the contributions due to the line energies of the isolated steps are much smaller by comparison. Finally, on the scale of the first two contributions, the effects due to the step–step interactions appear entirely negligible. As illustrated in the next section, the relative proportions of these three contributions are rather different for the case of interface dislocations.

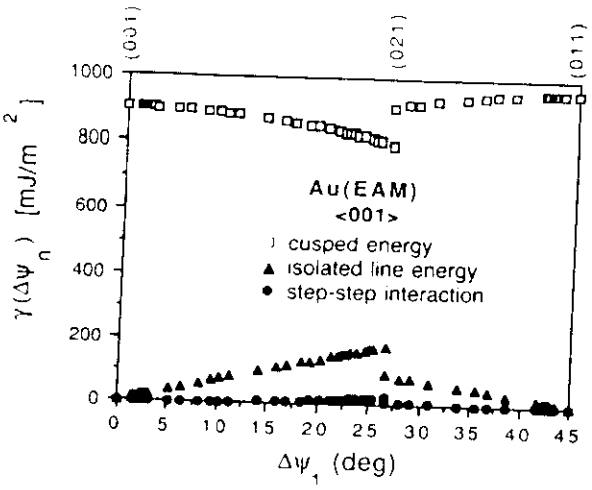

Fig. 26.17 Comparison of the relative magnitudes of the three contributions in eq. (26.55) to the free-surface energy, plotted separately against $\Delta\psi_1$ for both types of steps.

26.4.2 Grain boundary dislocations

To compare the core and strain-field energies of steps with those of dislocations, we now analyze the GB results in a similar manner. For simplicity, as in the case of the steps we again limit ourselves to interfaces in Au perpendicular to an ⟨001⟩ tilt (or pole) axis.

According to Fig. 26.5(a), two major cusped orientations, associated with the (100) and (110) planes, are encountered when rotating about a ⟨001⟩ tilt axis. As discussed elsewhere [7, 20], the STGBs on these two planes are identical to the related perfect-crystal configurations, with consequently vanishing cusped energies, by contrast with free surfaces and RGBs (Fig. 26.5(a)). By contrast to the free surfaces, however, for both the STGBs and RGBs several minor cusps appear between these major cusps; particularly noticeable are the ones associated with the (310) and (210) planes. These additional cusps, positioned in the 'high-angle' region of the two major cusps, make it exceedingly difficult to reliably extract core energies for the underlying main dislocations, particularly since we have no information on how these minor cusps affect the background energy associated with the main cusps. Moreover, as in the case of the steps one might contemplate consideration of additional vicinal STGBs, i.e. nearer to the bottoms of the two main cusps and hence far from these minor cusps. Unfortunately, however, because of the total domination for small values of $\Delta\psi$ of the strain-field over the dislocation-core contribution (as evidenced by the well-known logarithmic shapes of GB cusps; see for example, eq. (26.20b) and Fig. 26.5(a)), consideration of more-vicinal STGB planes provides no more information on the magnitude of the core energy.

To nevertheless gain some insight into the relative magnitudes of the core and strain-field contributions to the GB energy, we have performed a least-squares fit of the Read–Shockley equation (26.20b) to the simulation data for the STGBs in Fig. 26.5(a). Values thus obtained for the line energy, Λ^∞, and for the strength of the dislocation–dislocation interaction, $L_{el}^{d\text{-}d}$, are listed in Table 26.7. How well these parameters represent the actual simulation data for the two types of dislocations is illustrated in Fig. 26.18, which also shows the breakdown of the total energy in eq. (2.20b) (solid lines, with the simulation data of Fig. 26.11(a) superimposed) into the dominating contribution due to the dislocation–dislocation interaction and the one associated with their line energy (dotted lines).

Because of the particular pairwise geometrical grouping of the edge dislocations in STGBs (with mutually opposite Burgers vectors; Fig. 26.3), the line energies listed in Table 26.7 are thought to be governed by the dislocation **cores**. A comparison with the corresponding line energies of the steps in Table 26.6, Γ^∞/d, shows that the latter are typically three to four times larger than the core energies, Λ^∞/b, of the dislocations. Because of the weakness of the step–step interaction, it appears reasonable

Table 26.7 Dislocation parameters determined for the Au (EAM) potential (in units of mJ/m^2)

Tilt axis	*Cusped plane*	*Burger's vector, b/a*	Λ^∞/b	$L_{el}^{d\text{-}d}/b$
⟨100⟩	(100)	0.5	80 ± 25	960 ± 90
⟨100⟩	(110)	0.3535	110 ± 25	800 ± 80

to assume that the total line energy of the steps, $\Gamma^{s} = \Gamma^{s}_{core} + \Gamma^{s}_{el}$ (eq. (26.12)), is also dominated by the core energy. The magnitude of the ratio, $(\Lambda^{s}/b)/(\Gamma^{s}/d) \approx 0.25-0.35$ obtained from Tables 26.10 and 26.11 therefore indicates a significantly larger core energy of the steps than of the dislocations.

If the above interpretation is correct, this value for $(\Lambda^{s}/b)/(\Gamma^{s}/d)$ should be comparable in magnitude to the related core–energy ratios, $(\Lambda^{s}_{core}/b)/(\Gamma^{s}_{core}/h)$, determined in Figs. 26.7(a) and 26.9 from the direct simulation of the 'high-angle' interfaces, in which all elastic effects vanish, and which are listed in Table 26.3. The value of 0.33 obtained for the latter (for the Au(EAM) potential; Table 26.3) is in remarkable agreement with the above results, suggesting that (i) the line energies are, indeed, governed by the core contributions and (ii) the core energies of GB dislocations are substantially lower than those of surface steps.

A comparison between Figs. 26.17 and 26.18 shows another fundamental difference between GBs and free surfaces. While in the STGBs (Fig. 26.18) the elastic interaction energy vastly outweighs the core energy [8], the opposite is true for the free surfaces, in which the elastic contribution to the line energy is negligible compared to the core contribution (Fig. 26.17). As discussed further in the next section, this difference is responsible for the fact that a broken-bond model is so successful for free surfaces while for internal interfaces its usefulness is limited to the 'high-angle' limit in which elastic effects are irrelevant.

We conclude by pointing out that the vastly different amounts of elastic energy associated with the strain fields of GB dislocations, on the one hand, and surface steps, on the other, by comparison with the corresponding core energies have important consequences for the fracture behavior of internal interfaces in general. When fracturing an interface situated in the vicinity of an energy cusp, elastic work has to be done to convert the long-range strain fields near the dislocations into the short-range strain fields near the steps. When fracturing a **high-angle** boundary, by contrast, no sizeable elastic work has to be performed because the strain-field energies in both the GB and free surface are negligible due to the virtually complete core overlap. Among the three types of interfaces defined in section 26.2.4, the 'high-angle' interfaces therefore represent the group with the smallest work of adhesion, followed by the 'vicinal' and finally the 'cusped' or 'special' interfaces.

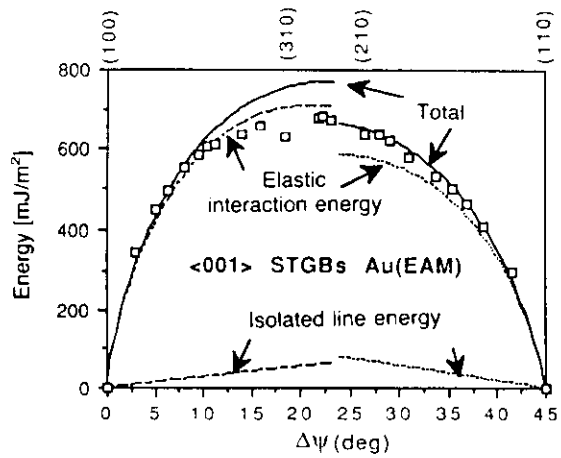

Fig. 26.18 Comparison of the relative magnitudes of the line energy and elastic–interaction energy contributions to the total GB energy in the Read–Shockley eq. (26.20b) (solid lines). The values for the line energy, Λ^{s}, and for the strength of the dislocation–dislocation interaction, L^{d-d}_{el}, obtained from a least-squares fit of eq. (26.20b) to the simulation data in Fig. 26.5(a) (squares), are listed in Table 26.7.

26.5 A BROKEN-BOND MODEL FOR INTERFACIAL DECOHESION

In the discussion of the role of broken bonds in section 26.2.5 it was argued that the energies of surfaces and interfaces, and therefore the work of adhesion, may be decomposed into a broken-bond contribution – associated with the cores of steps and dislocations in addition to those of the cusps – and the elastic energy of interaction between these line defects. To study the role of broken bonds, in all our simulations the *nn* and 2nd-*nn* miscoordination coefficients defined in eq. (26.29) were determined. Their analysis in this section will enable us to test the underlying basic assumptions, and to investigate the limitations of a broken-bond model for interfacial decohesion.

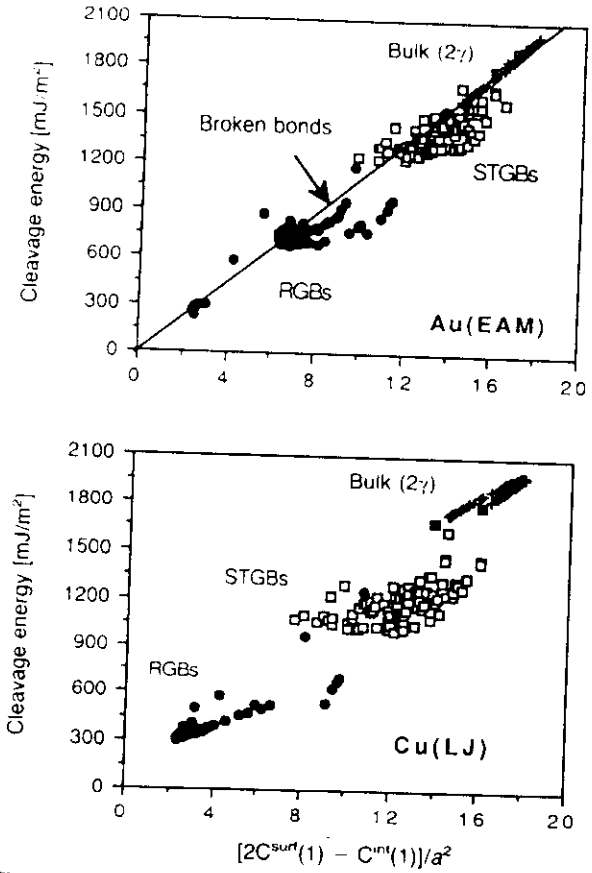

Fig. 26.19 Simulation data for STGBs, RGBs, and bulk perfect-crystal cleavage (2γ) obtained by means of the two fcc potentials against miscoordination difference, $(2C^{surf}(1, \Delta\psi) - C^{int}(1, \Delta\psi))$, between the two fracture surfaces and the internal interface (eqs. (26.44) and (26.45a)).

26.5.1 Work of adhesion

According to eq. (26.17a), the contribution to the work of adhesion due to bond breaking should be governed by the difference in the number of bonds broken in the two free surfaces and in the internal interface. To investigate the validity of this prediction, in Figs. 26.19(a) and (b) all the simulation data for STGBs, RGBs, and bulk cleavage (2γ) obtained by means of the two potentials are plotted against $[2C^{surf}(1, \Delta\psi) - C^{int}(1, \Delta\psi)]$. As seen from the figure, both the GB and free-surface energies are, indeed, reasonably well correlated with the difference in nearest-neighbor miscoordination, although the GB data scatter systematically towards smaller cleavage energies. By contrast, the scatter of the free-surface energies alone is much smaller; the scatter in this case was shown to disappear completely when the breaking of 2nd-*nn* bonds is also considered in the analysis [19].

As discussed in section 26.2.5, the total work of adhesion contains, in addition to broken bonds, an elastic contribution due to the conversion of the long-ranged dislocation strain fields into the short-ranged strain fields surrounding the steps (eq. (26.44)). However, following our discussion in sections 26.4.1 and 26.4.2, for all the vicinal interfaces the (negative) contribution in eq. (26.44) due to the dislocations dominates over the positive contribution due to the steps. Consequently, for the same number of broken bonds a 'vicinal' interface has a lower work of adhesion than either a 'special' or a 'high-angle' interface. The vicinal interfaces therefore appear to be the reason for the systematic scatter of the GB data in Figs. 26.19(a) and (b) towards lower energies. A broken-bond description of interfacial decohesion (see, for example, the solid line in Fig. 26.19(a)) therefore represents an upper limit for W^{ad}, with the elastic effects in vicinal interfaces causing a lowering of the work of adhesion due to bond breaking alone.

26.5.2 Broken bonds in steps and dislocations

In the discussion of the role of broken bonds in section 26.2.5 it was argued that the relatively small elastic displacements of the atoms situated near steps and dislocations should not appear in the miscoordination per unit interface area, $C(\alpha, \hat{n})$, defined in eq. (26.29). In writing eqs. (26.36) and (26.42) it was therefore assumed that only the cores of the steps and dislocations cause additional broken bonds over the cusped interfaces and, hence, contribute to $C(\alpha, \hat{n})$. In the following, this assumption will finally be tested.

Starting with the free surface, and recalling that for the Au(EAM) potential the 2nd-nearest-neighbor contribution to the surface energy is negligibly small [19], in Fig. 26.20 we have plotted the coordination difference (eq. (26.32)),

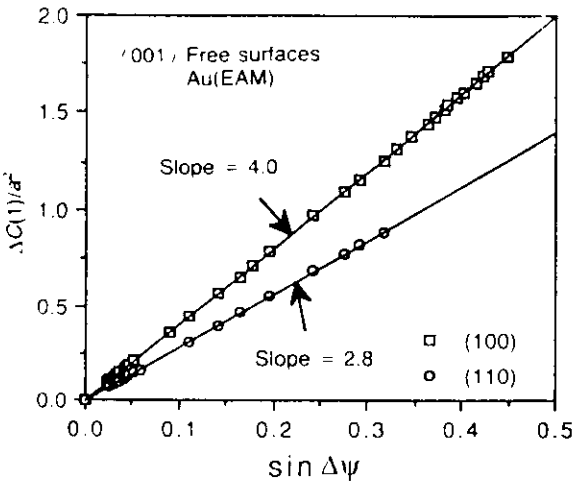

Fig. 26.20 Coordination difference, $\Delta C(1)/a^2$, defined in eq. (26.57) against $\sin\Delta\psi$ for the two steps considered in detail in section 26.4.1. The slopes of the solid lines, $C_{step}(1)/h$, obtained from a least-squares fit through the origin, are listed in Table 26.8.

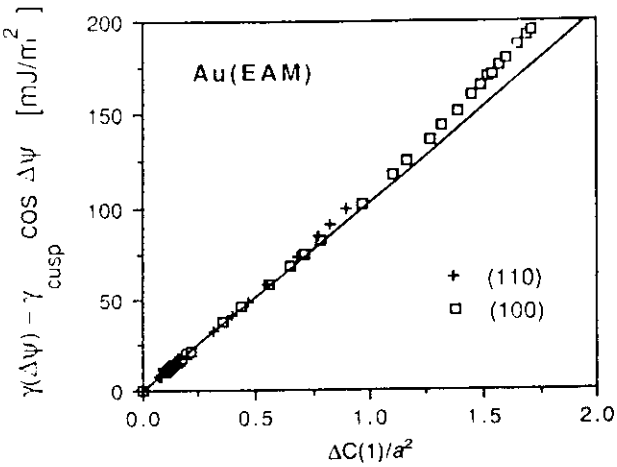

Fig. 26.21 Total energy increase from the cusp, $\gamma(\Delta\psi) - \gamma_{cusp}\cos\Delta\psi$ (eq. (26.11b)) against $\Delta C(1)$ from Fig. 26.20. The slight upwards curvature of the simulation data arises from the fact that only the cores of the steps give rise to broken bonds.

Table 26.8 Nearest-neighbor broken-bond parameters defined in section 26.2.5 (eqs. (26.32) to (26.35)) for the two steps considered in section 26.4.1 for the Au (EAM) potential (Fig. 26.20)

Pole axis	*Cusped plane*	*h/a*	$C^{surf}_{cusp}(1)/a^2$	$C_{step}(1)/(ha^2)$
⟨100⟩	(100)	0.5	8.00	4.0
⟨100⟩	(110)	0.3535	8.48	2.8

$$\Delta C(1) \equiv C^{surf}(1, \Delta\psi) - C^{surf}_{cusp}(1)\cos\Delta\psi \doteq [C_{step}(1)/h]\sin\Delta\psi \qquad (26.57)$$

against $\sin\Delta\psi$ for the two steps considered in detail in section 26.4.1. The excellent linearity of the plots, with slopes $C_{step}(1)/h$ listed in Table 26.8, confirms that the additional number of broken bonds per unit area introduced into the cusped surface is governed by the total length of the steps in the vicinal surface.

To demonstrate that only the cores are responsible for the broken bonds, in Fig. 26.21 the related total-energy increase from the cusp, $\gamma(\Delta\psi) - \gamma_{cusp}\cos\Delta\psi$ (eq. (26.11b)), is plotted against $\Delta C(1)$ from Fig. 26.20. If both the step cores *and* their elastic strain fields would cause broken bonds, a perfectly linear plot would be expected in Fig. 26.20. However, the slight upwards curvature clearly evident in the figure is proof that not all of the energy increase can be accounted for by bond-breaking alone. Given that both the sign and magnitude of the deviation from linear behavior (the latter obtained from a detailed analysis of the simulation data) are in quantitative agreement with the repulsive step–step interactions in Figs. 26.15 and 26.16, we conclude that, indeed, only the cores of the steps give rise to broken bonds.

It is interesting to note that the different slopes obtained in Fig. 26.20 for the (100) and (110) steps scale quantitatively with the corresponding line energies, Γ^∞/h, listed in Table 26.7, with the larger energy per unit height of the (100) steps giving rise to a proportionally larger number of broken bonds. This leads to the virtual overlap of the (100) and (110) data in Fig. 26.21, which represents further proof for the validity of a broken-bond description of the core energies, independent of the origin of the broken bonds.

To perform a similar analysis for the GB dislocations, in Fig. 26.22 we have plotted the coordination coefficients determined for the ⟨001⟩

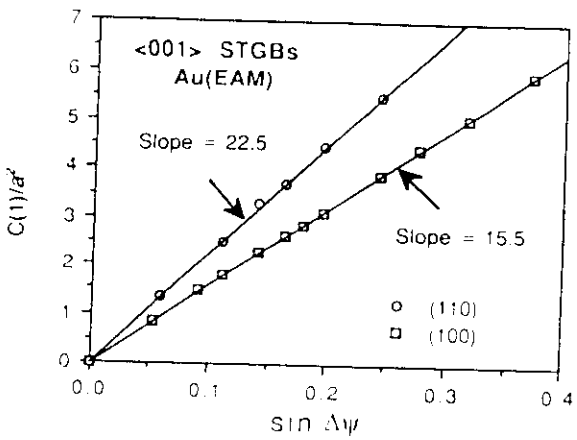

Fig. 26.22 Coordination coefficients, $C(1)/a^2$, for the (001) STGBs in Fig. 26.19, against $\sin\Delta\psi$ for the two types of dislocations considered in detail in section 26.4.2. The slopes of the solid lines, $C_{dis}(1)/h$, obtained from a least-squares fit through the origin, are listed in Table 26.9.

STGBs in Fig. 26.18 against sin $\Delta\psi$ for the two types of GB dislocations considered in section 26.4.2. Since the cusped energies vanish in this particular case (Fig. 26.18), according to eq. (26.57), $\Delta C(1) \equiv C(1)$. By contrast with Fig. 26.20, in Fig. 26.22 we have therefore plotted the total value of $C(1)$ against sin $\Delta\psi$. In accordance with eq. (26.32), Fig. 26.22 exhibits excellent linearity between the number of broken *nn* bonds per unit area and the total length of the dislocation cores in the different GBs. If the strain fields were to contribute broken bonds also, their contribution would be expected to be logarithmic rather than sinusoidal. We therefore interpret Fig. 26.22 as proof that only the dislocation **cores** cause broken bonds.

Table 26.9 Nearest-neighbor broken-bond parameters defined in section 26.2.5 (eqs. (26.36) to (26.38)) for the dislocations considered in section 26.4.2 for the Au (EAM) potential (Fig. 26.22)

Pole axis	*Step plane*	*b/a*	$C^{int}_{cusp}(1)/a^2$	$C_{dis}(1)/(ba^2)$
⟨100⟩	(100)	0.5	0.00	15.5
⟨100⟩	(110)	0.3535	0.00	22.5

As for the steps, the different slopes in Fig. 26.21 associated with the (100) and (110) steps scale quantitatively with the corresponding line energies, Λ^x/b, listed in Table 26.8, with the larger energy of the dislocations introduced into the (100) cusp giving rise to a proportionally larger number of broken bonds. While the cusped orientations have a very low degree of miscoordination in the GBs as compared to the free surfaces, it is interesting to note the much larger miscoordination per unit length of the dislocations compared to that of the steps (cf. Figs. 26.22 and 26.20). This result is particularly surprising if we recall the approximately three times larger line energy of the steps (cf. Tables 26.6 and 26.7). The origin of this apparent discrepancy is not understood yet; it appears, however, that the assumption of a single interaction-strength parameter, $\beta(a)$, for the relaxed cores of both steps (eq. (26.33)) and dislocations (eq. (26.39)) may be an oversimplification. The existence of broken bonds due to large elastic strains, as well as the relative contribution of higher-order-neighbor bonds, may also be of importance in the latter.

We finally mention that, in a sense, the broken-bond description discussed here may be viewed as little more than a quantified polyhedral-unit model [24]; while the structural units of a free surface are represented by the steps, the corresponding building blocks of the structure of an internal interface are the dislocation cores. Such structural-unit models have been criticized for their inability to (i) provide a quantifiable description of the interface structure and (ii) incorporate the systematic distortion of the structural units as a function, for example, of a steadily varying misorientation angle. Because the small elastic strains near steps and dislocations are usually not transmitted into broken bonds, the broken-bond model suffers from the same shortcoming in (ii) as do structural-unit models. However, by contrast with structural-unit models, a broken-bond description provides a quantitative characterization, in terms of the miscoordination per unit area of the related polyhedral building blocks, of the core contributions to various physical properties of the interface.

26.6 SUMMARY AND CONCLUSIONS

In this chapter we have taken the viewpoint that interfacial decohesion involves the transformation of the very long-ranged elastic strain fields near dislocations into the much shorter-ranged strain fields surrounding the surface steps. Our main goals have been to (i) formulate a comprehensive theoretical framework in which interfacial ideal-cleavage decohesion is viewed as the reversible transformation of misfit dislocations into surface steps, (ii) test the validity of the basic assumptions made in deriving the relevant expressions by means of atomistic computer simulations at zero temperature, and (iii) elucidate the distinct roles of broken bonds and of the elastic interactions between interface dislocations and surface steps during interfacial decohesion.

Within this framework, only the highly distorted core regions of the steps and dislocations were shown to give rise to broken bonds, while the overlapping elastic strain fields surrounding the two types of line defects are the source of their elastic interaction. Our simulations thus not only provide insight into the very different magnitudes of the elastic strain fields surrounding steps and dislocations, respectively, but also permit extraction of all relevant core parameters.

The main conclusions that have been drawn from our investigation may be summarized as follows.

1. The elastic strain-field energies per unit length of interface dislocations and surface steps differ dramatically. While the long-ranged elastic-interaction energy between dislocations shows the well-known logarithmic (Read–Shockley [8]) variation as a function of δ^{-1} (where δ is the separation between the line defects), the interaction between steps is of much shorter range, falling off proportionally to δ^{-2}. By comparison, the related core energies differ by much less, with the steps showing a typically two to three times larger core energy per unit length than the dislocations.
2. Depending on the relative magnitudes of the elastic strain-field energies by comparison with the related core energies, three types of internal interfaces and free surfaces may be distinguished, namely 'special', 'high-angle', and 'vicinal' interfaces. While the energies of both special and high-angle interfaces, and their work of adhesion, are dominated by the broken bonds, the behavior of vicinal interfaces, i.e. those in the vicinity of an energy cusp, is governed by both elastic and core effects. A broken-bond description of interfacial decohesion is therefore limited to special and high-angle interfaces.
3. A systematic investigation of the role of the interface plane demonstrates that the energies of surfaces and GBs on the **special**, i.e. most widely spaced, planes, and the ideal cleavage-fracture energy of the GBs, are governed by the interplanar lattice spacing, $d(hkl)$, parallel to the interface plane. By contrast, on the **vicinal** planes the value of $d(hkl)$ is irrelevant in both the energy and work of adhesion.
4. The comparison between interfacial and ideal-crystal brittle decohesion shows that **cusps** in the bulk ideal-crystal cleavage-fracture energy coincide with **peaks** in the GB work of adhesion. Responsible for this interesting behavior is the significantly smaller miscoordination of the **special** GBs as compared to the corresponding **flat** free surfaces.
5. Although the magnitudes of the works of adhesion of tilt and twist boundaries differ dramatically, the comparison of symmetrical tilt boundaries, which contain only edge dislocations, with high-angle twist boundaries, represented by the RGB model in which all screw-dislocation cores are assumed to overlap, shows a qualitatively similar behavior as far as core and elastic strain-field effects are concerned. This similarity suggests that our basic conclusions remain the same even when a twist component is added to a tilt component already present in the interface. The net effect is a lowering of the work of adhesion when screw dislocations are added to the edge dislocations.

In concluding we mention that, although the absolute values of GB and free-surface energies

presented throughout this paper are probably not very reliable when compared with experimental results, we hope that the comparison of the **relative** energies of GBs and free surfaces presented here is meaningful, particularly since throughout our investigation the same generic behavior was observed for conceptually rather different (pair versus many-body) interatomic potentials.

ACKNOWLEDGMENTS

We have benefited from discussions with Simon Phillpot and Sidney Yip. JAJ gratefully acknowledges support from the Office of Naval Research, under Contract No. N00014-88-F-0019. This work was supported by the US Department of Energy, BES-Materials Sciences under Contract W-31-109-Eng-38.

REFERENCES

1. See, for example, Chapter 25 in this volume.
2. A. A. Griffith, *Phil. Trans. R. Soc. Lond. A*, **221** (1920), 163.
3. See, for example, Chapter 2 in this volume.
4. See, for example, Chapter 3 in this volume.
5. See, for example, Chapter 4 in this volume.
6. See, for example, C. Herring, in *Structure and Properties of Solid Surfaces* (eds R. Gomer and C. S. Smith), University of Chicago Press (1953), p. 4, and references therein.
7. Chapter 1 in this volume.
8. W. T. Read and Shockley, *Phys. Rev.*, **78** (1950), 275.
9. D. Wolf, *J. Mater. Res.*, **5** (1990), 1708.
10. D. Wolf, *Phil. Mag. A*, **63** (1991), 1117.
11. A. P. Sutton, *Phil. Mag. A*, **63** (1991), p. 000.
12. M. S. Daw and M. I. Baskes, *Phys. Rev. B*, **29** (1986), 6443.
13. D. Wolf, *Physica B*, **131** (1985), 53.
14. D. Wolf, *Acta Metall.*, **37** (1989), 1983.
15. See, for example, P. G. Shewman and W. M. Robertson, in *Structure and Properties of Solid Surfaces* (eds R. Gomer and C. S. Smith), University of Chicago Press (1953), p. 67.
16. V. I. Marchenko and A. Y. Parshin, *Sov. Phys.-JETP*, 52 (1980), 129.
17. See, for example, C. Goux, *Can. Metall. Quarterly*, **13** (1974), 9.
18. D. Wolf, *J. Appl. Phys.*, **69** (1991), 185.
19. D. Wolf, *Surf. Sci.*, **226** (1990), 389.
20. D. Wolf, *J. de Physique*, **46** (1985), 197; D. Wolf and J. F. Lutsko, *Z. Kristallographie*, **189** (1989), 239.
21. S. A. Lindgren, L. Wallden, J. Rundgren and P. Westrin, *Phys. Rev. B*, **29** (1984), 576.
22. S. M. Foiles, M. I. Baskes, and M. S. Daw, *Phys. Rev. B*, **33** (1986), 7983.
23. D. Wolf, *Acta Metall. Mater.*, **38** (1990), 781.
24. M. Weins, H. Gleiter, and B. Chalmers, *Scripta Metall.*, **4** (1970), 235, and *J. Appl. Phys.*, **42** (1971), 2639.
25. T. W. Poon, S. Yip, P. S. Ho and F. F. Abraham, *Phys. Rev. Lett.*, **65** (1991), 2161.